


GLP-1R/GCGR dual agonism dissipates hepatic steatosis to restore insulin sensitivity and rescue pancreatic β -cell function in obese male mice

Received: 7 February 2024

Accepted: 29 April 2025

Published online: 21 May 2025

 Check for updates

A list of authors and their affiliations appears at the end of the paper

An early driver of Type 2 diabetes mellitus (T2D) is ectopic fat accumulation, especially in the liver, that impairs insulin sensitivity. In T2D, GLP-1R/GCGR dual-agonists reduce glycaemia, body weight and hepatic steatosis. Here, we utilize cotadutide, a well characterized GLP-1R/GCGR dual-agonist, and demonstrate improvement of insulin sensitivity during hyperinsulinemic euglycemic clamp following sub-chronic dosing in male, diet-induced obese (DIO) mice. Phosphoproteomic analyses of insulin stimulated liver from cotadutide-treated mice identifies previously unknown and known phosphorylation sites on key insulin signaling proteins associated with improved insulin sensitivity. Cotadutide or GCGR mono-agonist treatment also increases brown adipose tissue (BAT) insulin-stimulated glucose uptake, while GLP-1R mono-agonist shows a weak effect. BAT from cotadutide-treated mice have induction of UCP-1 protein, increased mitochondrial area and a transcriptomic profile of increased fat oxidation and mitochondrial activity. Finally, the cotadutide-induced improvement in insulin sensitivity is associated with reduction of insulin secretion from isolated pancreatic islets indicating reduced insulin secretory demand. Here we show, GLP-1R/GCGR dual agonism provides multimodal efficacy to decrease hepatic steatosis and consequently improve insulin sensitivity, in concert with recovery of endogenous β -cell function and reduced insulin demand. This substantiates GLP-1R/GCGR dual-agonism as a potentially effective T2D treatment.

Type 2 diabetes mellitus (T2D), commonly linked with obesity, is a chronic metabolic disease characterized by insulin resistance and progressive failure of pancreatic β -cells to meet the insulin secretory demand, resulting in poor glycaemic control associated with a multitude of co-morbidities, including metabolic dysfunction-associated steatotic liver disease (MASLD)^{1,2}, diabetic kidney disease^{3,4}, and cardiovascular dysfunction⁵. Current treatment regimens include oral therapies such as the insulin sensitizers metformin and thiazolidinediones, SGLT2 inhibitors that increase glucose excretion, and DPP4

inhibitors that prevent the endogenous degradation of incretin hormones such as glucagon-like peptide 1 (GLP-1)⁶. In general, these therapeutic approaches significantly delay the progression of the disease but, with time, the demand on the β -cell ever increases and eventually the endogenous insulin secretion has to be supplemented with exogenous insulin therapy⁷. Approximately 50% of patients treated with oral therapies progress to insulin replacement, which then exacerbates weight gain and further complicates the disease. More recently, GLP-1 receptor agonists and GLP-1R/GIPR dual-agonists have

✉ e-mail: rhianna.laker@astrazeneca.com; christopher.rhodes@astrazeneca.com

been introduced as injectable therapies for T2D, which potentiates endogenous glucose-induced insulin secretion and slows gastric emptying for improved glycaemic control, as well as decreases appetite and food intake that consequently reduces body weight and further improves metabolic homeostasis. The long-term impact of the GLP-1R agonist class on diabetes progression will be an exciting outcome to follow.

Early detection of diabetes, indicated by fasting hyperglycemia, and subsequent early intervention is beneficial for delaying progress to overt T2D and significantly reduces the risk of cardio-metabolic co-morbidities and mortality^{8,9}. Early drivers of T2D associated with obesity include ectopic fat accumulation in peripheral tissues, particularly the liver, impairing insulin sensitivity, which then creates a greater demand on the β -cell to secrete higher levels of insulin to maintain suppression of hepatic glucose output and promote peripheral tissue glucose uptake. If left untreated, chronic build-up of ectopic fat exacerbates insulin resistance to a point that exceeds β -cell compensation, resulting in elevated blood glucose so that T2D ensues¹⁰. Therefore, early therapy targeting reduction in ectopic fat accumulation may be key to halting, even reversing, T2D onset and development of the associated, life-threatening, complications.

Dual-agonist peptides targeting the GLP-1 and glucagon receptors (GCGR) provide similar weight loss and glucose control as GLP-1R agonists in humans¹¹. However, the GCGR agonist component gives additional therapeutic benefits to liver co-morbidities of T2D, MASLD, and its progressive form, metabolic dysfunction-associated steatohepatitis (MASH). This occurs via dramatic reductions in liver fat content in both preclinical rodent MASH models and T2D patients with obesity^{11–13}. GCGR activation in hepatocytes results in inhibition of *de novo* lipogenesis as well as enhanced mitochondrial turnover and mitochondrial oxidative capacity, increasing hepatic energy expenditure¹³. Therefore, the dual-action of GLP-1R/GCGR agonists provides both metabolic and hepatic benefits, making them excellent therapeutic candidates for MASH patients. Here, we show that GLP-1R/GCGR dual agonism provides multimodal benefits, reducing liver ectopic fat and improving insulin sensitivity, resulting in recovery of endogenous β -cell function.

Liver ectopic fat content is a major predictor/risk factor for a patient to advance from prediabetes to overt T2D^{14–16}. Thus, reducing hepatic steatosis could be an effective therapeutic strategy for significantly delaying progression to T2D. We hypothesized that the GLP-1R/GCGR dual-agonist-induced reduction in liver ectopic fat content would effectively alleviate insulin resistance, resulting in reduced hepatic glucose output, improve glucose disposal and lower the demand for β -cell insulin secretion. To address this multimodal hypothesis, it was necessary to take a comprehensive experimental approach to address multiple organ systems in response to GLP-1R/GCGR dual-agonism. This included hyperinsulinemic euglycemic clamp studies to assess whole body and tissue-specific insulin sensitivity, unbiased phosphoproteomic analyses to investigate insulin phosphor-signaling mechanisms in the liver, isolated islet studies to measure pancreatic β -cell function as well as addressing an opportunistic finding in brown adipose tissue activity and adaptation. We performed these studies in diet-induced obese mice, which are a mild model of metabolic impairment to mimic the prediabetic condition. These studies utilized the GLP-1R/GCGR dual-agonist cotadutide (MED10382), to complement previous metabolic studies in mouse models^{13,17} and human clinical trials^{11,12,18–20}. Our findings suggest that GLP-1R/GCGR dual-agonists provide benefits to patients with obesity, T2D and MASH and can likely be quite effective in preventing T2D progression in patients with prediabetes, especially if also exhibiting hepatic steatosis.

Results

Sub-chronic GLP-1R/GCGR dual agonism improves whole body and hepatic insulin sensitivity in hyperinsulinemic euglycemic clamp in DIO mice

To first assess the sub-chronic effect of GLP-1R/GCGR dual-agonist on insulin sensitivity, we performed a hyperinsulinemic euglycemic clamp. Diet-induced obese mice (~45 g body weight (BW)) were dosed daily for 28 days with either vehicle, cotadutide (10 nmol/kg), liraglutide (5 nmol/kg; GLP-1R agonist) or g1437 (5 nmol/kg; a GCGR agonist) also known as IUB288^{21–24}. The doses of liraglutide and g1437 were chosen to reflect half the molar dose of cotadutide to gain insight into the relative contribution of GLP-1R and GCGR action of cotadutide. The selected doses resulted in noticeably different levels of BW loss between the groups (Fig. 1A). Compared to baseline, cotadutide induced ~15% and g1437 induced ~27% BW loss. This is in line with previous observations with g1437 and other glucagon agonists and is driven primarily by a reduction in fat mass^{21–24}. As expected with the selected sub-optimal dose, liraglutide-treated mice did not lose BW, remaining significantly lighter than vehicle controls, which gained ~9% BW over the dosing period (Fig. 1A).

A hyperinsulinemic euglycemic clamp was performed on day 29, 16 h after the final dose to avoid any direct effect of drug action, a time known to have undetectable serum bioactivity of cotadutide, liraglutide or g1437 from previous studies¹³. Fasting blood glucose was significantly higher in mice treated with g1437 compared to all other groups, likely due to lower insulin levels and the lasting effect of increased glycogenolysis and glycogen depletion in the liver, given the stability of this molecule (half-life of ~6 h)²¹ (Fig. 1C). Fasting glucose of cotadutide-treated mice trended lower than vehicle perhaps reflecting increased basal glucose excursion but failed to reach statistical significance (Fig. 1B). However, fasting insulin was significantly lower in cotadutide- and g1437-treated groups compared with vehicle (Fig. 1C) and remained significantly lower during the clamp, despite equal exogenous insulin infusion between the groups (Fig. 1C). In the case of chronic catabolic g1437-treatment, this likely reflects a negative energy balance under which endogenous insulin secretion is shut down^{10,25}. However, when GCGR agonism is balanced together with GLP-1R agonism in cotadutide, the catabolic effect of GCG is mitigated by the GLP-1 component being able to maintain adequate insulin production²⁶. Here, our observation of reduced insulin with cotadutide is more consistent with the chronic effect of this treatment in improving insulin resistance and reducing insulin secretory demand²¹. To maintain euglycemia, clamped at ~140 mg/dL (Fig. 1D), the cotadutide-treated group required a slightly higher glucose infusion rate (GIR) (Fig. 1E), resulting in significantly higher area under the curve compared to vehicle and g1437 (Fig. 1F). Fasting glucose disposal was significantly lower in g1437-treated mice compared to vehicle and liraglutide groups (Fig. 1G).

During the hyperinsulinemic euglycemic clamp cotadutide significantly increased glucose disposal compared with the vehicle-treated group (Fig. 1G), suggesting improved whole-body insulin sensitivity. It is important to interpret these data in the context of insulin levels, which was done by correlating glucose disposal with plasma insulin during fasting and clamp conditions (Fig. 1H). The shift of the curve to the left and steeper slope in the cotadutide- and g1437-treated groups suggests dramatic improvement of insulin action (Fig. 1H). In the cotadutide-treated group this is driven through both reduced insulin levels and increased glucose disposal, while in the g1437-treated group it is only driven by the lower insulin levels. Fasting hepatic glucose production was significantly lower in g1437-treated mice compared with vehicle and liraglutide groups (Fig. 1I). This observation could be explained by hypothesized depletion of glycogen stores, which would not be completely depleted after a 5 h fast but

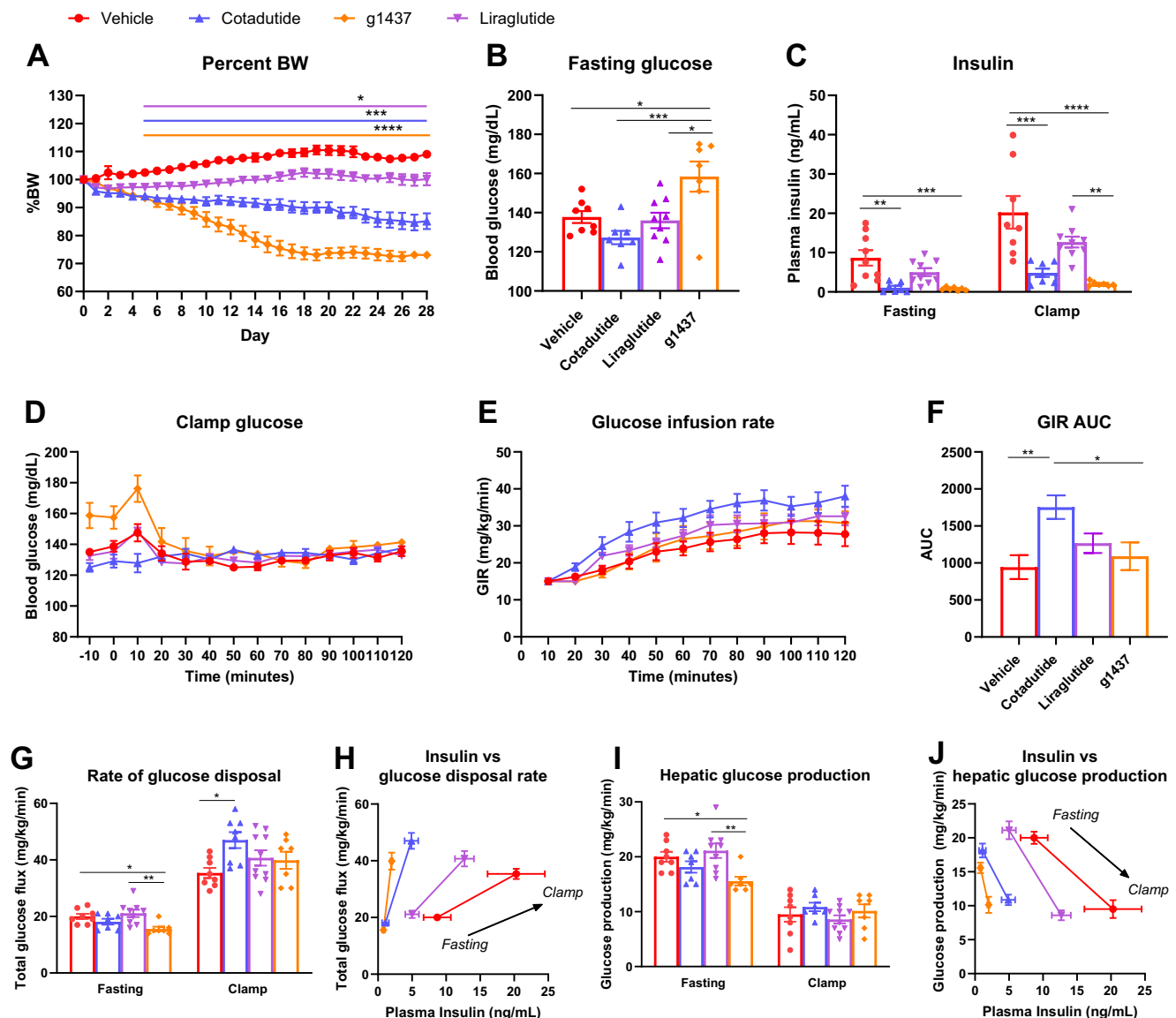


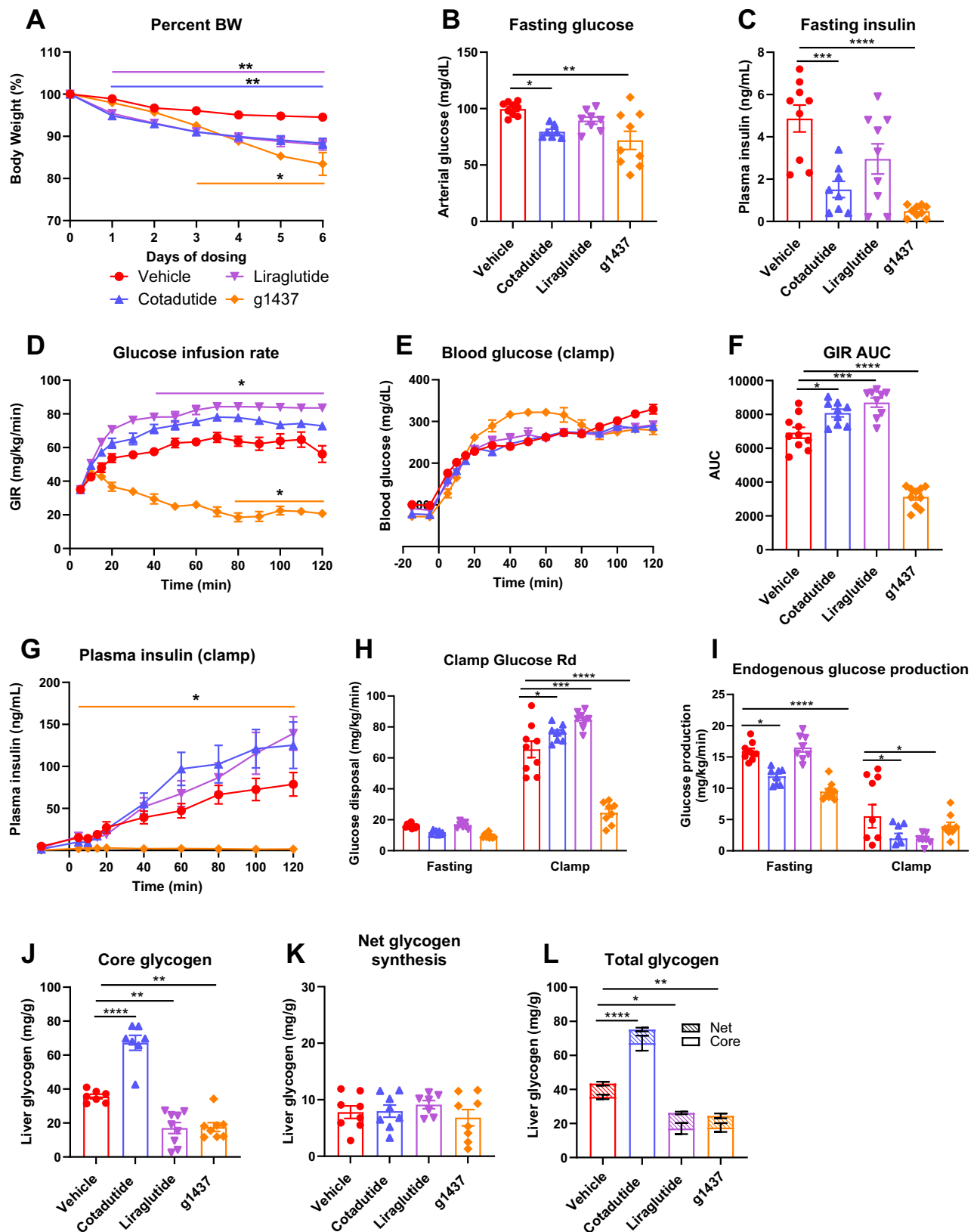
Fig. 1 | Cotadutide improves whole-body and hepatic insulin sensitivity in hyperinsulinemic euglycemic clamp in DIO mice. Metabolic parameters of DIO mice as assessed via a hyperinsulinemic euglycemic clamp following 28-day treatment of cotadutide (10 nmol/kg, blue upward triangles), liraglutide (5 nmol/kg, purple downward triangles), or g1437 (5 nmol/kg, gold diamonds) compared to vehicle (red circles). Reduction in body weight (BW) throughout the 28-day dosing period is shown as % change (A). Fasting blood glucose prior to clamp (B). Plasma insulin levels during fasting or clamp conditions (C). Blood glucose profile over time during clamp (D). Glucose infusion rate (GIR) (E) and the area under the glucose curve (AUC) (F) over time during the clamp. Rate of glucose disposal

during fasting or clamp conditions (G) and plotted against the corresponding plasma insulin levels (H). Hepatic glucose production during fasting or clamp conditions (I) and plotted against the corresponding plasma insulin levels (J). Vehicle ($n = 9$), cotadutide ($n = 8$), liraglutide ($n = 10$), g1437 ($n = 8$). Data shown as the mean \pm SEM. In (A), lines above the graph indicate differences compared with the vehicle at each time point and correspond to the respective group color. Two-way ANOVA with Tukey's multiple comparisons post hoc (A), One-way ANOVA with Tukey's multiple comparisons post hoc (B, C, F, G, I). * $p < 0.05$, ** $p < 0.01$, *** $p < 0.001$, **** $p < 0.0001$. Exact p values are included in the Source Data file. Source data are provided as a Source Data file.

with the additional action of g1437 to induce glycogenolysis and subsequently a reduction in liver glycogen may exacerbate the reduction in liver glycogen stores leading to impaired glucose output. Indeed, the liver still maintains some glucose output, which is reflected in the higher fasting glucose levels but is not controlled through insulin secretion. Hyperinsulinemia during the clamp induced similar suppression of hepatic glucose production between all groups (Fig. 1I). When interpreted in the context of insulin levels (Fig. 1J), however, we again report a shift of the cotadutide and g1437 curves to the left, suggesting improved hepatic insulin action in these groups driven by the lower insulin levels (Fig. 1J).

Short-term GLP-1R/GCGR dual agonism results in normal insulin secretory capacity during hyperglycemic clamp in DIO mice

Having assessed insulin sensitivity using the hyperinsulinemic euglycemic clamp, we next sought to examine the impact of cotadutide on insulin secretory capacity and β -cell function in response to hyperglycemia. To this end, a hyperglycemic clamp in DIO mice treated with vehicle, cotadutide, liraglutide, or g1437 for 7 days was conducted in the absence of exogenously administered insulin, prior to potential BW loss adaption. In order to match the BW loss across all groups compared to control, equimolar doses (10 nmol/kg) were used in this experiment. As expected, this resulted in similar BW loss between



treatment groups compared with control, given the shorter time course (~12–17% BW loss from baseline; Fig. 2A).

The clamp experiment was performed on day 8, 16 h after the final dose. Cotadutide and g1437 groups displayed significantly reduced fasting glucose and insulin compared with vehicle, while liraglutide-treated animals were not different from the vehicle-treated group

(Fig. 2B, C). Hyperglycemia was clamped between 250 and 300 mg/dL (Fig. 2D) with g1437-treated mice requiring dramatically lower GIR compared to all other groups (Fig. 2E, F), explained by negligible insulin secretion and severely impaired glucose disposal (Fig. 2G, H). Again, this likely reflects a catabolic negative energy balance induced by chronic g1437 mimicking a prolonged fasted state that shuts down

Fig. 2 | Cotadutide-treated DIO mice have normal insulin secretory capacity in response to hyperglycemia. Metabolic parameters of DIO mice as assessed via a hyperglycemic clamp following 7-day treatment of cotadutide (10 nmol/kg, blue upward triangles), liraglutide (10 nmol/kg, purple downward triangles), or g1437 (10 nmol/kg, gold diamonds) compared to vehicle (red circles). Reduction in body weight (BW) throughout the 7-day dosing period is shown as % change (A). Fasting blood glucose (B) and fasting plasma insulin (C) prior to the clamp. Glucose infusion rate (GIR) (D), blood glucose levels (E), the area under the glucose curve (AUC) (F), and plasma insulin levels (G) during clamp conditions. Glucose disposal (Rd) under fasting and clamp conditions (H). Endogenous glucose production under

fasting and clamp (I). Baseline (core) glycogen levels prior to clamp (J), net glycogen synthesis during clamp (K), and total glycogen at the end of the clamp (L). Vehicle ($n = 10$), cotadutide ($n = 9$), liraglutide ($n = 9$), g1437 ($n = 10$). Data are shown as the mean \pm SEM. In (A, D, G), lines above the graph indicate differences compared with the vehicle at each time point and correspond to the respective group color. Two-way ANOVA with Tukey's multiple comparisons post hoc (A, D, G), One-way ANOVA with Tukey's multiple comparisons post hoc (B, C, F, H–L). * $p < 0.05$, ** $p < 0.01$, *** $p < 0.001$, **** $p < .0001$. Exact p values are included in the Source Data file. Source data are provided as a Source Data file.

endogenous insulin production^{10,25}. Note the dose differences for g1437 between the hyperinsulinemic clamp of 5 nmol/kg (Fig. 1) and the hyperglycemic clamp of 10 nmol/kg (Fig. 2), which may exacerbate the observations to the hyperglycemia. Meanwhile, liraglutide-treated mice required significantly higher GIR (Fig. 2E), with cotadutide showing intermediate GIR which became significant when AUC was calculated (Fig. 2F). Both liraglutide and cotadutide groups had similar and expected potentiation of glucose-induced insulin secretion (Fig. 2G) with both groups displaying significantly higher glucose disposal compared with vehicle (Fig. 2H).

At baseline, endogenous glucose production was lower in cotadutide and g1437 groups compared with vehicle (Fig. 2I). During the hyperglycemic clamp, all groups had suppressed glucose production, with cotadutide and liraglutide significantly lower than vehicle (Fig. 2I). Baseline 'core' glycogen was elevated above vehicle in cotadutide-treated mice, as previously observed¹³, but significantly lower in the liraglutide- and g1437-treated groups compared to the vehicle control group (Fig. 2J). Net glycogen synthesis during the clamp was similar between all groups (Fig. 2K). As such, differences in total glycogen at the end of the clamp (Fig. 2L), reflected that of the "core" glycogen (Fig. 2J). Collectively, these clamp data demonstrate that both cotadutide and liraglutide maintain normal insulin secretion in response to hyperglycemia and improve insulin sensitivity, manifested by enhanced glucose disposal and suppression of hepatic glucose production in response to equivalent insulin levels.

GLP-1R/GCGR dual-agonism enhances hepatic insulin-stimulated signaling pathways in DIO mice

We hypothesized that the improvement of hepatic insulin sensitivity by GLP-1R/GCGR dual-agonism, as shown in Fig. 1J, is associated with enhanced insulin signaling in the liver. This idea was examined further by treating DIO mice with either vehicle or cotadutide for 28 days and 16 h after the final dose, and then administered a single intraperitoneal bolus of PBS or insulin (0.75 U/kg). After 15 min, livers were harvested and clamp-frozen for subsequent proteomic and phosphoproteomic analyses (Fig. 3A). Cotadutide significantly reduced liver lipid content as assessed by NMR, as well as microvesicular and macrovesicular steatosis (Supplementary Fig. 1A–F). In line with this, cotadutide-treated mice had significantly smaller livers compared to vehicle-treated mice (Supplementary Fig. 1B), although when normalized to body weight was not different to vehicle (Supplementary Fig. 1C). For the proteomic analyses, comparison was made between the cotadutide + PBS group (CP) with the vehicle + PBS (VP) group, given that there would be negligible changes of the total proteome within just 15 mins of acute insulin stimulation. Cotadutide-treatment induced notable proteomic alterations, with 531 significantly up- and 431 significantly downregulated hepatic proteins (Fig. 3B and Supplementary Data 1). These differential protein levels were enriched predominately for metabolic processes including carbon/amino acid metabolism, fatty acid/cholesterol metabolism, glucose/glycogen turnover, and insulin/glucagon signaling as supported by KEGG pathway analysis (Fig. 3C). Key proteins differentially regulated by cotadutide in the insulin signaling network included the insulin receptor (INSR), RAS,

mTORC1 up- and down-stream components, (DEPTOR, LAMTOR1, LARPI, RPS6, TSC1, PRKAB1), regulators of PI3K signaling (INPP1L, INPP5F, and PIK3C2A), and regulators of glycogenesis/glucose (GCKR, GYG2, PPP1R3G, PHK and PYGL) (Fig. 3B and Supplementary Data 1). These changes are supported by our previous transcriptomics analysis in a murine MASH model treated with cotadutide¹³, producing an overlap of 205 of the differentially expressed proteins, including similar changes in fatty acid metabolism molecules (HSD17B12, LPL, CES1G and CES2C) and insulin signaling (INPP5F and PRKAB1). For phosphoproteomic analyses, the basal level of phosphorylation was set as the vehicle + PBS (VP) group and the phosphoproteome compared to the vehicle + insulin (VI) phosphoproteome (representative of prediabetic insulin-resistant state), and cotadutide + insulin (CI) phosphoproteome (representative of improved hepatic insulin sensitivity (as assessed during clamp studies)) (Fig. 3A). Cotadutide-treatment resulted in 2004 significantly upregulated phosphopeptides in response to insulin (CI/VP) compared to 1262 in the VI group (VI/VP), with 1032 phosphopeptides shared between them (Supplementary Fig. 2A and Supplementary Data 1). An analogous number of downregulated phosphopeptides was also observed between these groups with a similar degree of overlap (Supplementary Fig. 2A). CI/VP phosphopeptides not overlapping with VI/VP mapped to proteins key in the insulin signaling pathway as supported by KEGG analysis (Supplementary Fig. 2B). This effect was not observed for VI/VP phosphopeptides that did not overlap with CI/VP, or the shared sites (Supplementary Fig. 2B). To determine how both vehicle and cotadutide insulin-stimulated groups differed we compared the fold-change between CI and VI treated conditions (CI/VI). Here, there were ~750 up- and down-regulated phosphopeptides in CI/VI that mapped to proteins enriched in the insulin signaling pathway based on KEGG analysis (Supplementary Fig. 2A, B).

Known elements in insulin signaling pathways were probed to understand how cotadutide modulated specific insulin-stimulated phosphopeptides at the molecular level. We observed differential phosphorylation of critical adapter proteins at the insulin receptor. This includes SOS1 that had increases in known insulin-stimulated phosphorylation sites^{27,28} in CI compared to VP or VI (S1147, S1196) (Fig. 4A and Supplementary Data 1). ARAF also showed increased phosphorylation at S255, associated with protein activation²⁹, in CI compared to VI and decreased phosphorylation at S186 in both groups. Most notably, insulin-receptor substrate-2 (IRS2) had multiple significantly upregulated phosphosites in CI compared to VI (T517, T524, S556, S573, S616, S907, and S1089) many of them among the topmost upregulated of all 747 phosphosites (e.g., fifth and seventh), an effect not observed with insulin-receptor substrate-1 (IRS1; Fig. 4A and Supplementary Data 1). Although IRS1 and 2 proteins were not detected in the proteomic analyses in this study, we have previously observed increases in IRS2, but not IRS1, at the protein and RNA level with 28 days of cotadutide-treatment (Supplementary Fig. 2C). Downstream of IRS1/2, the PI3K signaling pathway also demonstrated differential phosphorylation in CI compared to VI. PTEN antagonizes PI3K signaling and had increases in de-stabilizing phosphosites (T366; mediated by GSK-3 and S370; mediated by CK-2) and decreases in stabilizing phosphosite S385^{30,31}. PIK3C2A also demonstrated

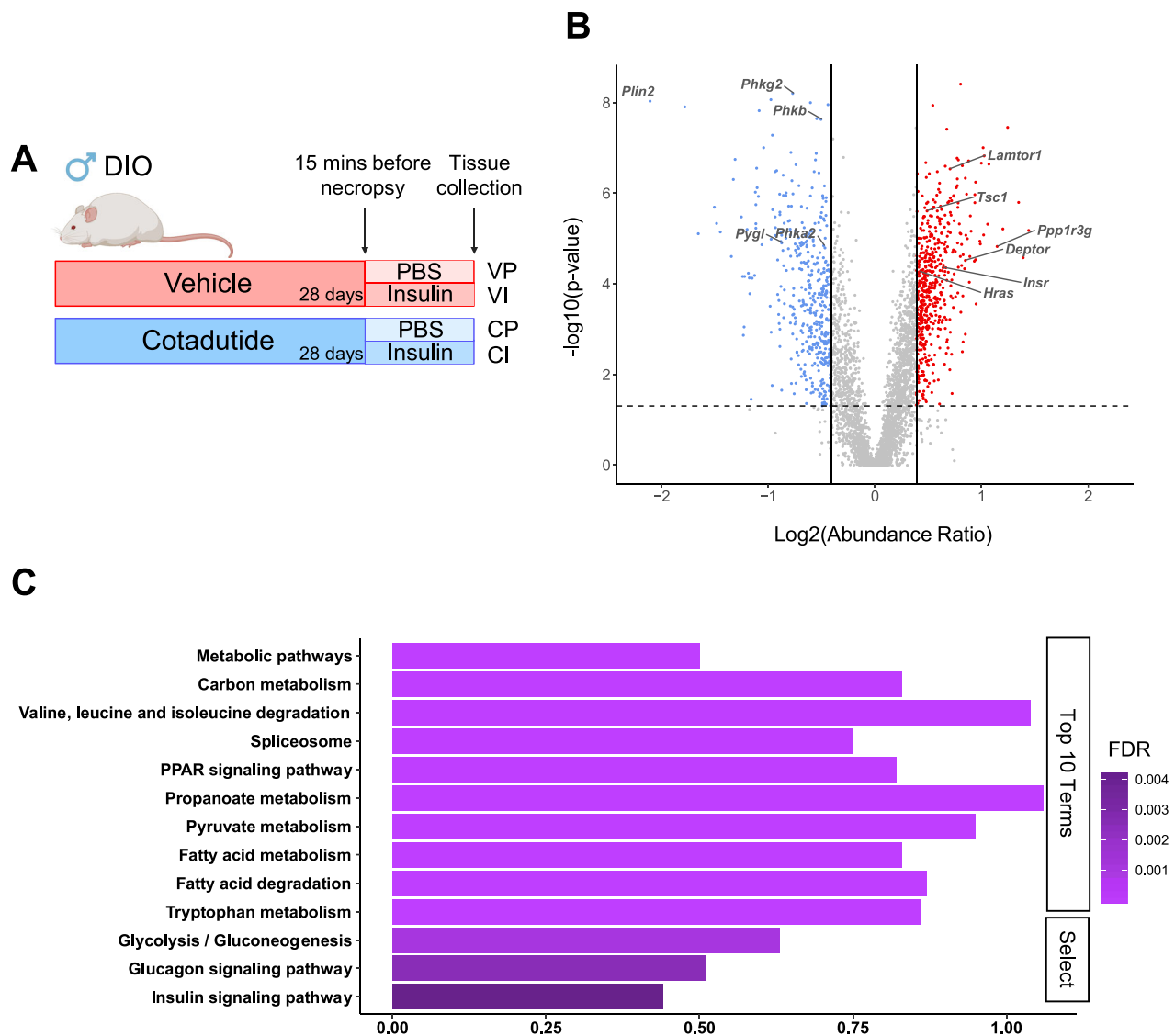


Fig. 3 | Cotadutide induces changes in the hepatic proteome of metabolism-related proteins in DIO mice. Experimental design for proteomic and phosphoproteomics study in which DIO mice were treated with cotadutide or vehicle for 28 days, then injected with PBS or insulin yielding four groups: vehicle + PBS (VP), vehicle + insulin (VI), cotadutide + PBS (CP), and cotadutide + insulin (CI). Created in BioRender. Kajani, S. (2025) <https://BioRender.com/t03r158> (A). Volcano plot of significant up- (red, 531) or down-regulated (blue, 431) hepatic proteins comparing

CP/VP as identified via proteomics (B). KEGG pathway analysis of all significantly differentially regulated hepatic proteins comparing CP/VP (C). $n = 4$ mice per group. In (B), dashed line denotes $p = 0.05$ and solid lines mark cut-off values for abundance ratio < 0.76 or > 1.315 . The in-built one-way ANOVA statistical test in Proteome Discover (PD) was used to generate p values. In (C), KEGG term ranking based on FDR and significance based on FDR < 0.05 . Source data are provided as a Source Data file.

increased phosphorylation at an insulin-stimulated site (S261)³² (Fig. 4A and Supplementary Data 1). Although we did not identify any change in protein levels or direct modifications of PDK1, these upstream phosphorylation changes may indicate an increase in PDK1 activity.

A limitation of phosphoproteomic analyses is that not all phosphopeptides are necessarily detected. Indeed, we did not detect phosphorylation of AKT in response to insulin stimulation in our phosphoproteomic dataset. Therefore, we performed a western blot for known insulin signaling phosphorylation sites of AKT as validation. Without insulin stimulation, cotadutide reduces phosphorylation of AKT on S473, a potential feedback mediated by GCGR agonism. We identified robust phosphorylation of AKT on S473 with CI compared to VI or VP, but not on Thr308 despite potential activation of PDK1, which regulates Thr308 phosphorylation³³ (Fig. 4B and Supplementary

Fig. 2D). This specific AKT phosphorylation profile has been reported by others as essential for GCGR-agonist mediated improvement in insulin sensitivity and a key component of GCGR and INSR signaling crosstalk^{34–37}. Supporting this, the most significantly upregulated CI/VI phosphosite was on PPP1R3G at S81 (Fig. 4A and Supplementary Data 1). PPP1R3G is a phosphatase critical for promoting glycogenesis during the fasting-feeding transition and is phosphorylated by AKT in response to insulin stimulation^{38,39}. AKT mediated phosphorylation of PPP1R3G promotes its activity and dephosphorylation of its targets, most notably glycogen synthase 2 (GYS2)³⁹. GYS2 dephosphorylation increases its activity to promote glycogenesis. We observed decreased phosphorylation of GYS2 with CI compared to VI at S8, the most critical site regulating its activity, among others (S8/T10, S627, S645, and S657)⁴⁰ (Fig. 4A and Supplementary Data 1). Phosphorylase kinase (PHK) also demonstrated cotadutide-dependent decreased

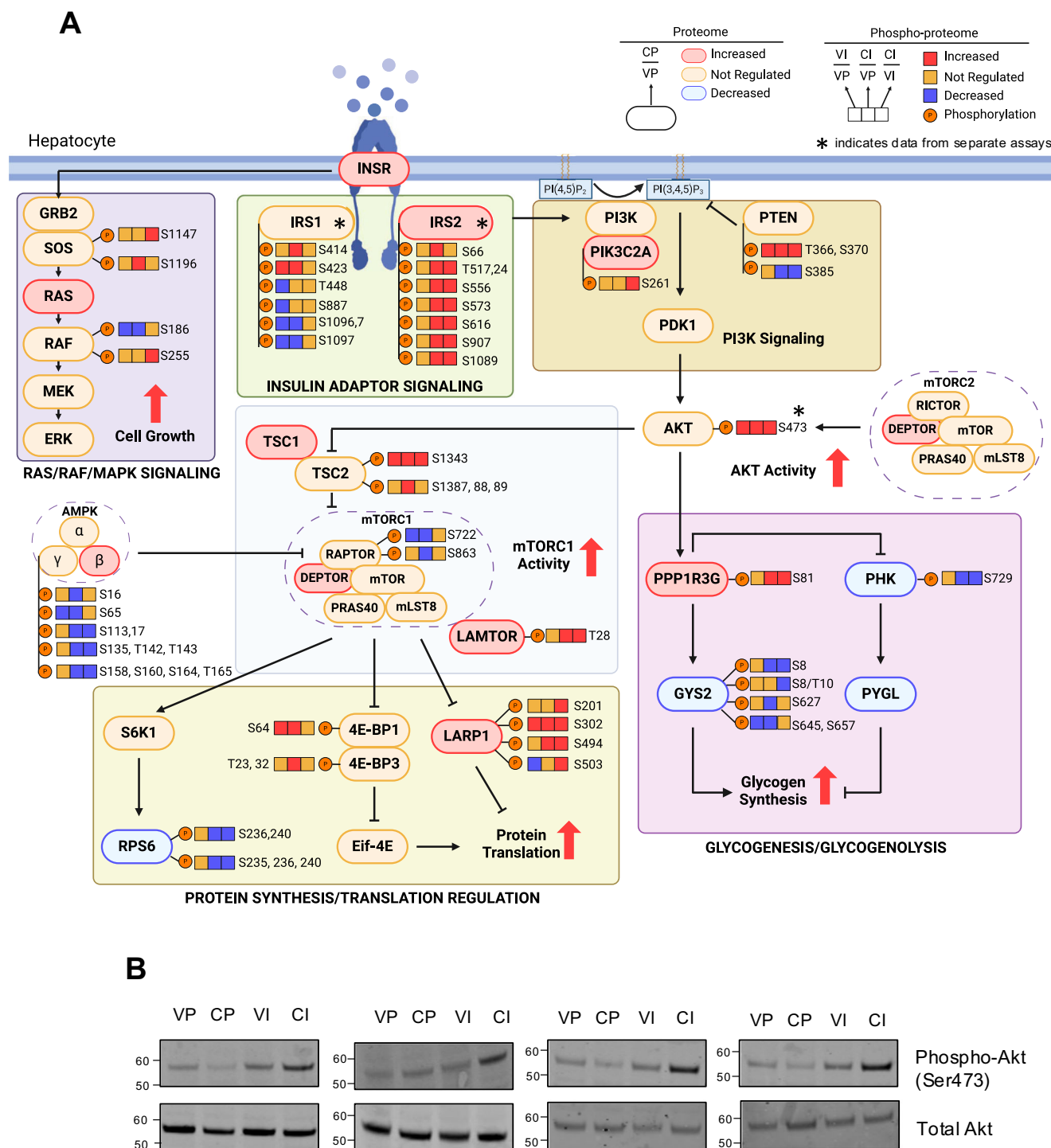


Fig. 4 | Cotadutide enhances hepatic insulin-stimulated signaling pathways in DIO mice. Schematic depicting proteomic and phosphoproteomics changes in the insulin signaling pathway based on the experimental design described in Fig. 3A including comparisons (detailed further in figure key) between the following groups: vehicle + PBS (VP), vehicle + insulin (VI), cotadutide + PBS (CP), and cotadutide + insulin (CI). Due to space limitations, selected phosphosites are shown. *Indicates data derived from immunoblot or separate proteomic studies as noted in text. The full list of phosphosites is detailed in Supplementary Data. Created in

BioRender. Kajani, S. (2025) <https://BioRender.com/t41v037> (A). Immunoblot of phosphorylated AKT at serine 473 from the groups described in Fig. 3A compared to total AKT (B). $n = 4$ mice per group. In (A, B), increased or decreased proteomic or phosphoproteomics changes based on $p < 0.05$ and abundance ratio < 0.76 or > 1.315 , or $p < 0.01$ and abundance ratio < 0.76 or > 1.315 , respectively. The in-built one-way ANOVA test in Proteome Discover (PD) was used to generate p values. Source data are provided as a Source Data file.

phosphorylation (S729) with insulin, thought to dampen antagonism of glycogenesis by glycogen phosphorylase (GP)⁴¹ (Fig. 4A and Supplementary Data 1). Collectively, these phospho-changes are predicted to enhance insulin-stimulated postprandial glycogenesis and glucose control in cotadutide-treated mice.

Also downstream of AKT, the mTORC1 regulators TSC2 (S1343, S1387, S1388, and S1389) and LAMTOR1 (T28) both had increased phosphorylation in CI compared to VI or VP (Fig. 4A and Supplementary Data 1). AKT mediated serine phosphorylation of TSC2 has been shown to be essential for insulin-stimulated

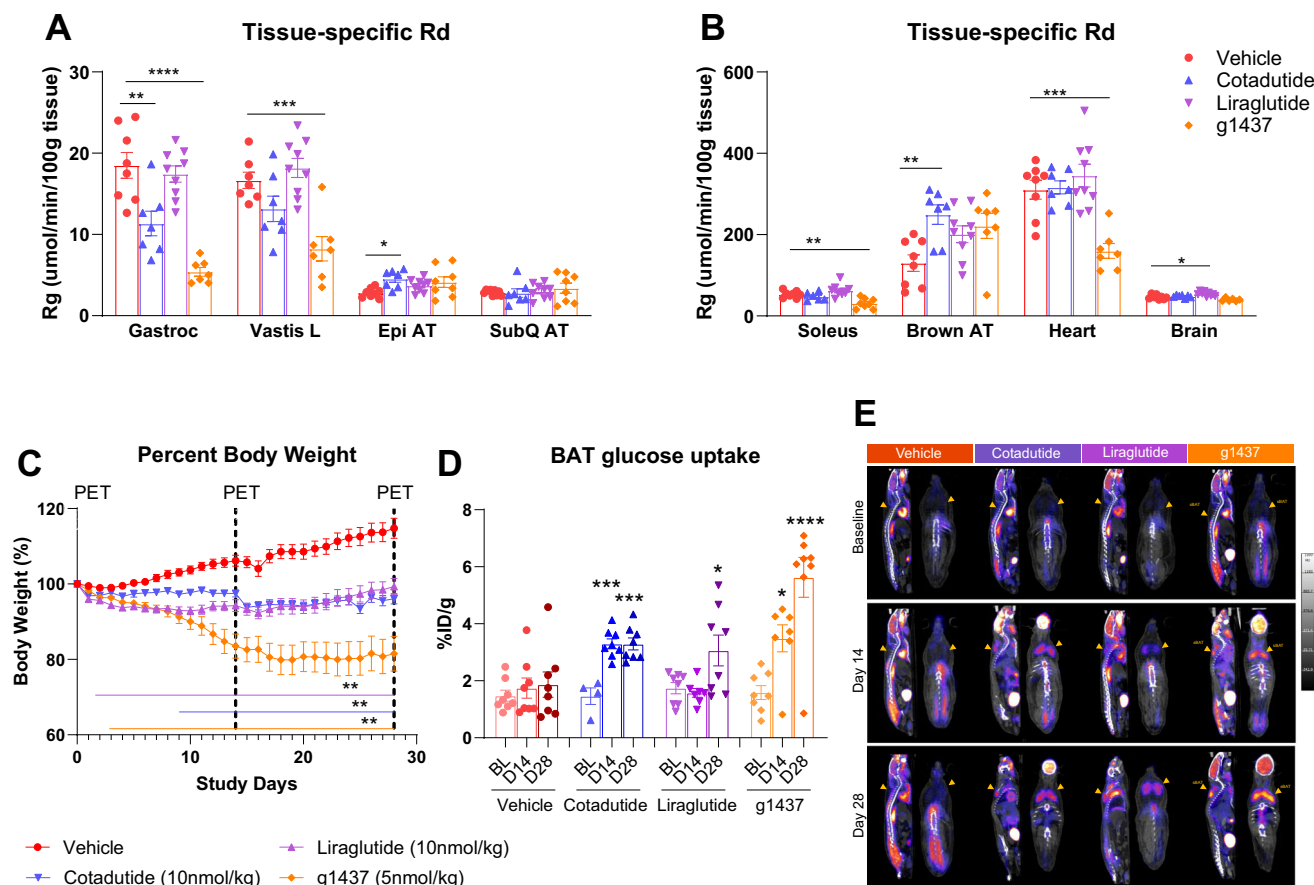


Fig. 5 | Cotadutide increases brown adipose tissue glucose uptake. Analysis of glucose uptake in DIO mice following 28-day treatment of cotadutide (10 nmol/kg, blue upward triangles), liraglutide (5 nmol/kg, purple downward triangles) (A, B), 10 nmol/kg (C–E), or g1437 (5 nmol/kg, gold diamonds), compared to vehicle (red circles). Tissue-specific glucose uptake (Rd) in gastrocnemius (Gastroc), vastus lateralis (Vastus L), perigonadal adipose tissue (PG AT), subcutaneous adipose tissue (SubQ AT) (A), soleus muscle, brown adipose tissue (Brown AT), heart, and brain tissue (B). Vehicle ($n = 9$), cotadutide ($n = 8$), liraglutide ($n = 9$), g1437 ($n = 8$). Reduction in body weight (BW) throughout the 28-day dosing period is shown as % change, with fluorodeoxyglucose (FDG) positron emission tomography (PET) imaging timepoints indicated (C). $n = 8$ mice per group. Quantification of FDG-PET

glucose uptake measurements in brown adipose tissue (BAT) at baseline, day 14, or day 28 of treatment (D). Representative image from FDG-PET studies summarized in (D), (E). $n = 8$ mice per group, except cotadutide baseline ($n = 4$), liraglutide D14 ($n = 7$), g1437 D14 ($n = 7$). Data shown as the mean \pm SEM. In (C), lines below the graph indicate differences compared with a vehicle at each time point and correspond to the respective group color. One-way ANOVA with Tukey's multiple comparisons post hoc for each tissue (A, B) or each treatment group (D). Two-way ANOVA with Tukey's multiple comparisons post hoc (C). * $p < 0.05$, ** $p < 0.01$, *** $p < 0.001$, **** $p < 0.0001$. Exact p values are included in the Source Data file. Source data are provided as a Source Data file.

mTORC1 signaling, albeit at different serine sites to those identified in the current report^{42,43}. RAPTOR had decreased phosphorylation of the AMPK-mediated inhibitory S722 site, loss of which activates mTORC1⁴⁴, in both insulin-treated conditions. AMPK had a global decrease in phosphorylation on the regulatory gamma subunit (PRKAG2) in CI compared to VI or VP (Fig. 4A and Supplementary Data 1). Downstream of mTORC1, LARP1 phosphorylation was broadly increased (S201, S302, S494, S503) in CI compared to VI, which is expected to prevent its inhibition of protein translation^{45,46} (Fig. 4A and Supplementary Data 1). 4E-BP1 showed similar increased phosphorylation (S64) with insulin stimulation in both vehicle and cotadutide groups, that is associated with increased protein translation⁴⁷. Finally, p70S6K is a downstream target of mTORC1 that phosphorylates RPS6 to enhance translation⁴⁸. However, RPS6 had decreased phosphorylation in CI compared to VI and VP (S236, S240, S235, S236, and S240), departing from the classical insulin-stimulated response (Fig. 4A and Supplementary Data 1). Together, these integrated proteomic and phosphoproteomic data suggest that cotadutide-induced improvement in hepatic insulin sensitivity is mediated through altered and/or improved insulin signaling pathways.

GLP-1R/GCGR dual agonism increases brown adipose tissue glucose uptake in DIO mice through glucagon action

In addition to identifying improvements in hepatic insulin sensitivity during the hyperinsulinemic euglycemic clamp, we also showed improved insulin sensitivity in relation to glucose disposal. As part of the same clamp study, we assessed insulin-stimulated glucose uptake in other insulin-sensitive peripheral tissues. At 120 min during the hyperinsulinemic euglycemic clamp (Fig. 1), mice were administered a bolus of 2-deoxyglucose and individual tissues collected 35 min later for assessment of insulin-stimulated tissue-specific glucose uptake (Fig. 5A, B). Glucose uptake in the gastrocnemius muscle was lower in cotadutide- and g1437-treated mice vs. vehicle (Fig. 5A). Reduced glucose uptake was also observed in the vastus lateralis and soleus muscles as well as the heart with g1437 treatment (Fig. 5A, B). These reductions in skeletal and cardiac muscles are likely contributed by the lower insulin levels observed in these groups (Fig. 1C). Tissue-specific glucose uptake in the liraglutide-treated mice was not different to vehicle in all tissues measured except a rather small, but significant, increase in the brain (Fig. 5B). Interestingly, we observed a significant increase in glucose uptake in brown adipose tissue (BAT) and epididymal adipose tissue (EpiAT) in cotadutide-treated mice

compared with vehicle (Fig. 5B). The preferential increase in BAT glucose uptake is quite notable considering the larger scale of the effect between EpiAT (~ 2.5 $\mu\text{mol}/\text{min}/100$ g tissue) and BAT (~ 120 $\mu\text{mol}/\text{min}/100$ g tissue).

We confirmed this finding in two independent cohorts of mice via FDG-PET imaging at thermoneutrality with the same treatment duration and dose (Fig. 5C–E and Supplementary Fig. 3A–D). At thermoneutrality, confounding BAT activation due to housing mice at sub-optimal temperatures is minimized, therefore more directly linking any observed BAT activation to pharmacological intervention. In one of these studies (Fig. 5C–E), we included treatment groups for liraglutide and g1437 and adjusted the dose of liraglutide (10 nmol/kg) to achieve similar BW between cotadutide and liraglutide (Fig. 5C), to appreciate a weight dependent and independent effect of BAT glucose uptake. We maintained g1437 at a dose of 5 nmol/kg which resulted in significantly greater BW loss compared to all other groups (Fig. 5C). FDG-PET was performed at baseline, day 14 and day 28 of dosing. Both g1437 and cotadutide increased BAT glucose uptake robustly after 14 d of dosing, which was maintained at the 28-day time point (Fig. 5D, E) and occurred in all mice in the cotadutide-treated group. Conversely, liraglutide, achieved elevated BAT glucose uptake only at 28 days of dosing, with the effect only observed in 50% of mice in this group that did not correlate with BW and is therefore likely an indirect consequence (Fig. 5D). Our previous studies demonstrated increases in energy expenditure in mice treated with cotadutide¹⁷. Although not directly measured in this study, energy expenditure increases are frequently accompanied by increases in body temperature. Consistent with this, in a separate experiment in which doses of liraglutide, cotadutide and g1437 were adjusted throughout the study to result in equal BW after 28 days (Supplementary Fig. 4A) we also observed an increase in body temperature in cotadutide-treated animals, with a similar trend observed in the g1437-treated group (Supplementary Fig. 4B). These increases in body temperature support the idea that cotadutide may increase energy expenditure via activation of BAT in mice.

To further characterize this improvement in BAT metabolism, we performed transcriptomic analysis, electron microscopy, and histological analysis on the BAT. RNA sequencing revealed 1609 upregulated and 1714 downregulated genes in BAT from cotadutide-treated mice compared with vehicle-treated control mice (Fig. 6A, B). Key genes that were upregulated in BAT following cotadutide treatment included interferon regulatory factor 4 (*Irf4*; a transcriptional activator associated with increased thermogenic gene expression^{49,50}), complement factor D (*Cfd*, also known as Adipsin; an adipokine shown to improve pancreatic β -cell function^{51,52}), CCAAT enhancer binding protein delta (*Cebpd*; a transcriptional activator important for mitochondrial biogenesis⁵³ and thermogenesis⁵⁴), cytochrome c oxidase subunit 8b, subunit 7a and subunit 4 isoform 1 (*Cox8d*, *Cox7a*, *Cox4l1*; terminal enzyme of the electron transport chain), cell death inducing DNA fragmentation factor alpha-like effector A (*Cidea*; a lipid droplet associated protein that promotes lipid storage⁵⁵) and adiponectin, C1Q and collagen domain containing (*Adipoq*; an adipokine involved in fat metabolism and insulin sensitivity) (Fig. 6A). Interesting downregulated genes include leptin (*Lep*; an adipokine with a major role in regulation of energy homeostasis), fatty acid desaturase 3 (*Fads3*; introduces double bond to unsaturate fatty acids), sterol-coA desaturase (*Scd1*; plays a role in lipid biosynthesis), C-C motif chemokine ligand 2 (*Ccl2*; a ligand for chemokine receptor CCR2) and tumor necrosis factor (*Tnf*; a pro-inflammatory cytokine) (Fig. 6A). Gene ontology enrichment analysis revealed that cotadutide upregulated multiple metabolism-related gene ontologies including fatty acid metabolic processes, mitochondrial organization and respiratory chain complex related ontologies (Fig. 6B). This phenotype becomes even more apparent in the histological images, which show increased UCP-1 in BAT from

cotadutide-treated mice compared to vehicle (Fig. 6C). H&E analysis (Fig. 6D) also showed significantly reduced pathologist-assessed microvesicular score in BAT from cotadutide-treated mice compared to vehicle controls (Fig. 6E). Electron microscopy images were quantified and revealed reduced fat droplet area and size in BAT from cotadutide-treated mice (Fig. 6F, G, J) as well as increased mitochondrial area, but similar mitochondrial size between cotadutide- and vehicle-treated BAT (Fig. 6H–J).

FGF21 is a known insulin-sensitizing agent that is secreted from the liver and can activate energy-expenditure programs in BAT. Chronic cotadutide-treatment in DIO mice increased the expression of hepatic *Fgf21* as revealed by qRT-PCR (Supplemental Data 4), along with a tendency for increased serum FGF21 ($p = 0.07$) (Supplemental Data 4). A previous RNA-seq dataset from the liver of cotadutide treatment in a murine model of MASH also revealed increases of hepatic *Fgf21* expression with cotadutide (Supplemental Data 4) and suggests that FGF21 may play, at least in part, a role in cotadutide-induced BAT activation. Altogether, these results suggest that cotadutide, through a hepatic glucagon-driven mechanism, activates BAT to increase mitochondrial activity, resulting in the observed increase in BAT-specific glucose uptake.

GLP-1R/GCGR dual agonism-induced improvement in insulin sensitivity confers lower insulin secretory demand on the pancreatic β -cell

To examine whether the cotadutide-induced improvement in insulin sensitivity and glucose lowering confers changes in β -cell insulin secretory function and endocrine pancreas morphology, we treated 2 cohorts of DIO mice with vehicle or cotadutide for 28 days, which resulted in significantly lower BW ($\sim 20\%$) in cotadutide-treated mice (Fig. 7A), similar to our previous observations¹³. There was a similar pancreas weight between cotadutide- and vehicle-treated groups (Fig. 7B). In cohort 1, pancreatic islets were isolated and subjected to perfusion at basal glucose levels (2.8 mmol/L) followed by perfusion with media containing stimulatory glucose concentration (16.7 mmol/L) to induce an insulin secretory response. Perfusate was collected at 2 min intervals for 80 min to assess biphasic insulin secretion. Islets from vehicle-treated DIO mice demonstrated dramatically higher levels of glucose-stimulated insulin secretion indicative of an insulin-resistant condition requiring substantially more insulin to elicit a normal physiological response (Fig. 7C). In contrast, islets isolated from cotadutide-treated mice demonstrated much lower first and second phase insulin secretion in response to the same glucose stimulation (Fig. 7C), suggesting an adaptive improvement in insulin sensitivity for maintenance of glucose homeostasis. Importantly, this observation was not due to differences in pancreatic insulin content (measured in cohort 2) and was similar between the cotadutide-treated and vehicle control groups (Fig. 7D). Fasting insulin levels were also significantly lower in cotadutide-treated mice (Fig. 7E), further supporting an adaptive improvement of insulin sensitivity and thus lower insulin demand. Interestingly, we observed a reduction in pancreatic glucagon content (Fig. 7F) and fasting endogenous glucagon levels (Fig. 7G) in cotadutide-treated mice, which is likely a response to therapeutic glucagon agonist administration. We have previously observed reduced plasma glucagon in mice treated with therapeutic glucagon agonists, including cotadutide and g1437¹³. Both β -cell and α -cell mass was assessed histologically by insulin and glucagon staining. The β -cell mass was not significantly different between vehicle- or cotadutide-treated mice (Fig. 7H), but there was a significantly lower α -cell mass in cotadutide-treated mice (Fig. 7I). In the context of the pancreas, MAFA is a β -cell-specific transcription factor, and MAFA+ nuclei were significantly increased in the pancreas from cotadutide-treated mice (Fig. 7J).



immature granules (Fig. 7M) compared to the vehicle group, suggesting an improved functional secretory capacity with cotadutide treatment. Representative images are provided in Fig. 7N. This cotadutide-mediated change in β -cell insulin granule content is also indicative of an adaptive response to restore normal endogenous β -cell function as a consequence of improved insulin sensitivity¹⁰.

Fig. 6 | Cotadutide increases brown adipose tissue mitochondrial activity and content. Transcriptomic and histological analyses of brown adipose tissue (BAT) following 28-day treatment of cotadutide (10 nmol/kg, blue triangles), compared to vehicle (red circles). Volcano plot of genes significantly up- (red) or down-regulated (blue) by cotadutide in BAT as identified via RNA-seq. Vehicle ($n = 4$); Cotadutide ($n = 5$) mice per group (A). Gene ontology analysis for enriched biological process (red), molecular function (orange), or cellular component (yellow) for genes significantly upregulated by cotadutide in BAT (B). Representative images of immunohistochemical staining of BAT for UCP-1 (C) and H&E (D) of vehicle (top) and cotadutide (bottom). Vehicle ($n = 8$); Cotadutide ($n = 7$) mice per group. Quantification of BAT Score from H&E staining (E) Vehicle ($n = 8$); Cotadutide ($n = 7$) mice

per group. Quantification of histological parameters from electron microscopy imaging in J, including lipid droplet area (F), lipid droplet size (G), mitochondria area (H), and mitochondria size (I). Biologic replicates are $n = 2$ mice per group. Technical replicates are vehicle ($n = 10$) and cotadutide ($n = 19$) images per mouse. Representative images of electron microscopy imaging of vehicle (left) and cotadutide (right) BAT (J). Adjustments were made for multiple comparisons using the Benjamini–Hochberg adjustment. Genes with Benjamini–Hochberg false discovery rate < 0.05 as determined by DESeq2 were considered significant (A) two-sided Student's t -test (E–I). Data shown as the mean \pm SEM. * $p < 0.05$, ** $p < 0.01$, *** $p < 0.001$, **** $p < .0001$. Exact p values are included in the Source Data file. Source data are provided as a Source Data file.

Discussion

We have previously shown that the GLP-1 component of cotadutide drives BW loss and improves metabolic homeostasis, while the glucagon action drives liver-specific benefits to reduce steatosis through inhibition of lipogenesis and improved mitochondrial function, accompanied by the critical downstream consequences of reduce inflammation and fibrosis¹³ (Fig. 8). Liver-specific benefits of cotadutide have also been reported in T2D patients showing significantly reduced liver fat content by MRI-PDFF (magnetic resonance imaging-proton density fat fraction) as well as significant reductions in circulating collagen fragment, Pro-C3, as a biomarker for liver fibrosis activity and in the FIB4 index, a risk-factor score for fibrosis^{11,12,56–59}. Beyond this, cotadutide has shown to have additional benefits for diabetic kidney disease^{19,60,61}. Importantly, these therapeutic benefits are achieved by a precise balance of GLP-1R and GCGR agonism with a $\sim 5:1$ bias toward GLP-1¹⁷. In this way, the metabolic benefits of GCGR agonism can be leveraged without the undesired impacts on glucose control that are counteracted by sufficient GLP-1R agonism to drive weight loss and confer glucose control benefits. In the current report, we expand these findings to demonstrate further benefits of GLP-1R/GCGR dual-agonism to improve insulin sensitivity, increase BAT glucose uptake, and enhance BAT metabolic activity (Fig. 8). These metabolic improvements consequently facilitate a reduced demand for insulin production to then allow for β -cell rest and functional recovery (Fig. 8).

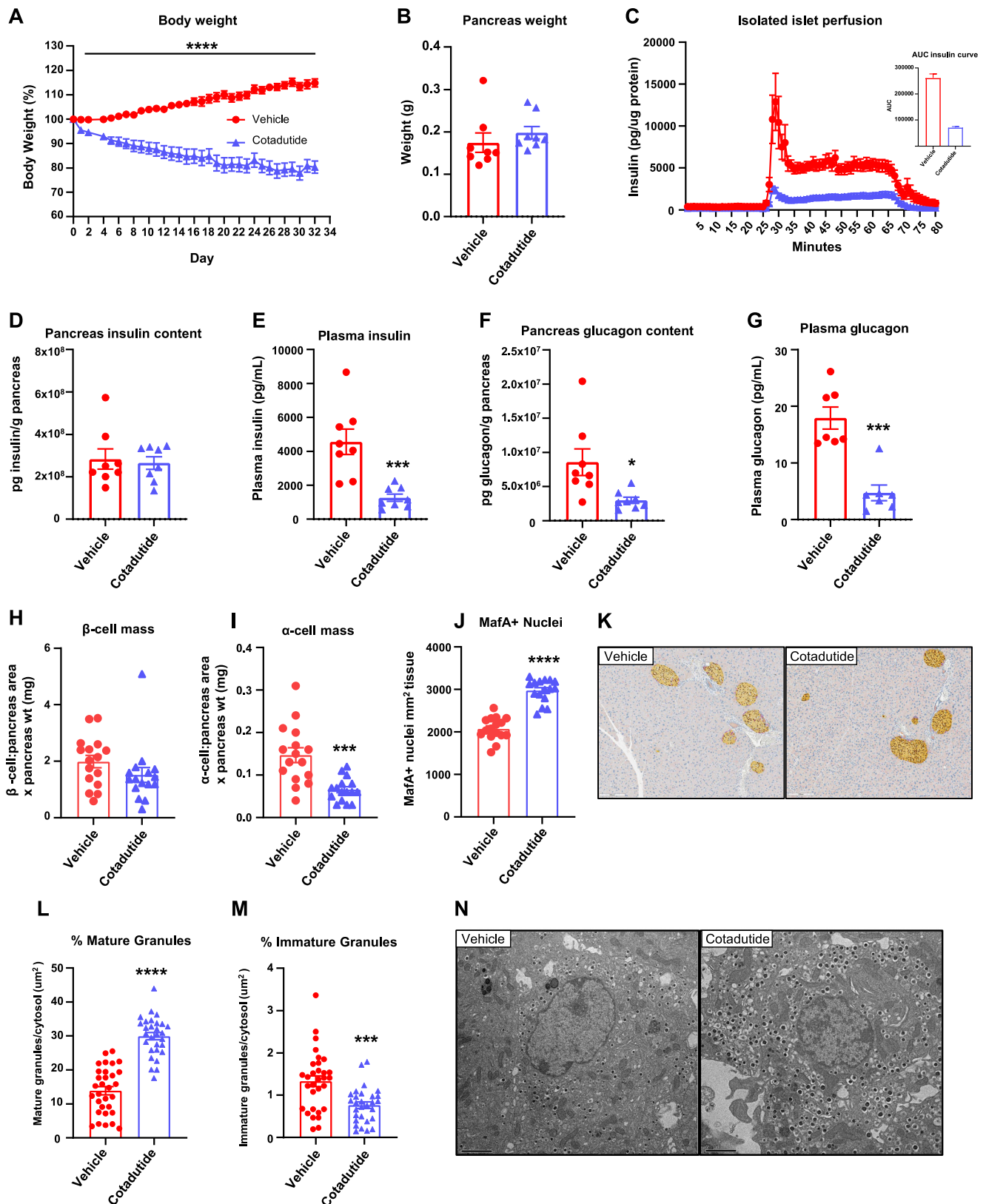
We employed the “gold-standard” hyperinsulinemic euglycemic clamp technique, which demonstrated that sub-chronic cotadutide treatment significantly improved insulin sensitivity. In this study, hepatic glucose production was suppressed to similar levels between all groups, but this was accompanied by dramatically lower insulin levels in the cotadutide- and g1437-treated groups, indicating an enhanced insulin sensitivity. This occurred in the groups receiving therapeutic glucagon, suggesting that this degree of glucagon treatment induces metabolic adaptation in the hepatocyte, resulting in an improved response to insulin stimulation. In the hyperglycemic clamp, it was confirmed that the suppression of hepatic glucose output is not necessarily due to glucagon-induced glycogen depletion, as was observed in the g1437 group but not in cotadutide-treated mice. Indeed, there is a consistent observation of elevated glycogen content following cotadutide treatment, which is most likely a rebound effect following a transient glycogen depletion observed around 6 h post-dose and reflective of cotadutide's half-life in mice¹³. Such fluctuations in the hepatic glycogen content are much less with liraglutide treatment and lower glycogen levels likely reflect GLP-1 induced reduction in food intake and body weight¹³.

It should be noted that the hyperglycemic clamp was performed after only 7 days of treatment, that resulted in an equivalent BW loss between the cotadutide, liraglutide, and g1437 groups. But similar to the hyperinsulinemic clamp, we found that both cotadutide and g1437 significantly lowered fasting insulin. However, during hyperglycemia, cotadutide, liraglutide, and vehicle control groups responded with normal increases of insulin secretion, while g1437-treated mice

were unable to mount an insulin secretory response. In this regard, it is important to consider that g1437 treatment simulates chronic glucagon exposure, which induces a chronic catabolic state akin to starvation. These states are known to severely dampen pancreatic β -cell function and insulin secretion through an unknown mechanism that is likely not directly mediated by glucagon agonism¹⁰. Exogenous glucagon may potentiate insulin secretion in experimental models^{50–52}, but this may be mostly mediated via the β -cell GLP-1 receptor⁵¹. However, the in vivo physiological consequence of glucagon action on β -cells remains uncertain, especially considering that directional flow through a pancreatic islet is from β -cells to α -cells, such that secreted glucagon has to complete a circuit of the body, including escaping clearance through the liver and kidney, so that minimal concentrations of glucagon actually reach the β -cell and are unlikely to have a physiological effect^{62,63}. Critically, the glucagon component in cotadutide does not show this catabolic effect, given that the balance of GCGR and GLP-1R activity within cotadutide has been optimized to achieve the specific benefits of glucagon-induced inhibition of hepatic lipogenesis, while still allowing for metabolic switching in response to glycemic status¹³. The findings reported here further support that an appropriate balance of GCGR and GLP-1R tone is also sufficient for improved metabolic control, during both hyperinsulinemic and hyperglycemic clamps, to maintain sufficient insulin secretion in response to hyperglycemia and suppression of hepatic glucose production.

The cotadutide-induced improvement of insulin sensitivity prompted a deeper molecular analysis of the hepatic proteome and insulin-regulated phosphoproteome. Cotadutide treatment enhanced multiple components of the hepatic insulin-stimulated signaling network, including insulin-receptor adapter protein phosphorylation, AKT activation, glycogen synthesis, cell growth, mTORC1 activation, and protein synthesis translation.

While glucagon is generally thought of as counter-regulatory to insulin, several studies have demonstrated hepatic GCGR and INSR crosstalk as essential for potentiating insulin action³⁷. For example, acute GCGR agonism enhances hepatic phosphorylation of AKT S473, but not T308, essential for glucagon-mediated improvements in insulin sensitivity^{34–36}. Further, glucagon-dependent induction of IRS2 expression shifts the IRS2:IRS1 ratio to favor IRS2 and is key for early insulin action during the fasting-feeding transition to suppress hepatic glucose output³⁶. These observations suggest that, in a normal physiological fasting state, glucagon primes insulin action. Our data support these observations and point to GCGR and INSR signaling partnership as a key component driving enhanced insulin signaling with cotadutide in DIO mice. Here, specific enhancement of hepatic AKT S473 phosphorylation, but not T308, with CI/VI and increased protein and gene expression of *Irs2*, but not *Irs1* by cotadutide treatment supports this concept and complements previous observations^{34–36}. Beyond this, the integrated proteomic and phosphoproteomics approach builds on these previous reports and provides a much more comprehensive picture of how glucagon primes insulin action in the liver. For example, our data implicate PPP1R3G as a critical component of this response. PPP1R3G had one of the largest



fold-change increases induced by cotadutide, and PPP1R3G S81 phosphorylation had the largest fold-change across all phosphosites when comparing CI/VI. Similar to IRS2, PPP1R3G expression peaks in the liver during the fasting-feeding transition and can be induced by glucagon treatment^{38,39}. Unlike other PPI phosphatase subunits, PPP1R3G is not allosterically inhibited by GP and can promote glycogen synthesis during the early phase of insulin action, upon

phosphorylation by AKT, allowing for rapid clearance of postprandial blood glucose levels³⁸. As such, increased PPP1R3G activity with cotadutide treatment may be essential for the enhanced insulin sensitivity observed and, more broadly, may be considered a previously unknown component of glucagon signaling in the priming of insulin action. Together, the above-mentioned differences in insulin-stimulated protein phosphorylation between cotadutide- and

Fig. 7 | Improved insulin sensitivity by cotadutide results in reduced insulin secretory demand on the pancreatic β -cell. Analysis of pancreatic function following 28-day treatment of cotadutide (10 nmol/kg, blue triangles), compared to vehicle (red circles). Reduction in body weight (BW) throughout the 28-day dosing period shown as % change ($n = 8$ mice per group) (A). Total pancreas weight ($n = 8$ mice per group) (B). Insulin levels in perfusate from isolated pancreatic islets across time (main) and the area under the curve (inset) ($n = 8$ mice per group) (C). Total pancreatic insulin content (D) or plasma insulin levels ($n = 8$ mice per group) (E). Total pancreatic glucagon content ($n = 8$ mice per group) (F) or plasma glucagon levels ($n = 7$ mice per group) (G). Quantification of β -cell mass (H), α -cell mass (I), or MAFA-positive staining nuclei (J) from multiplexed immunohistochemistry of

pancreata. Representative images of immunohistochemistry. Biologic replicates are $n = 8$ mice per group. Technical replicates are $n = 2$ images per mouse. K. Quantification of mature granules (L) or immature granules (M) from electron microscopy of pancreatic β -cell islets. Biological replicates are $n = 2$ mice per group. Technical replicates are $n = 29$ (cotadutide) and $n = 31$ (vehicle) β -cells imaged per mouse. Representative images of electron microscopy (N). Two-way ANOVA with Tukey's multiple comparisons post hoc (A), two-sided Student's t -test (B, C (inset), D–J, L, M). Data shown as the mean \pm SEM. * $p < 0.05$, ** $p < 0.01$, *** $p < 0.001$, **** $p < .0001$. Exact p values are included in the Source Data file. Source data are provided as a Source Data file.

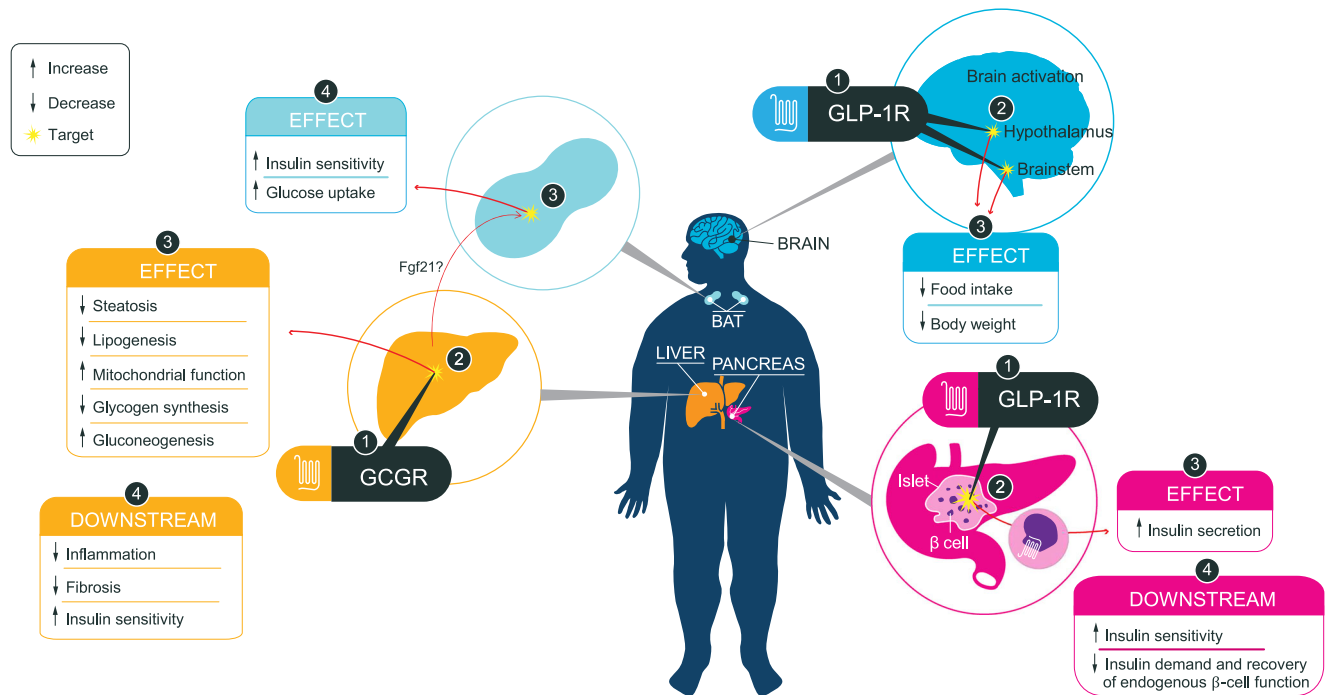


Fig. 8 | Updated summary of Cotadutide mechanism of action. Cotadutide-mediated GLP-1R agonism at the brain inhibits appetite, resulting in decreased food intake and body weight loss, while GCCR agonism at the liver reduces hepatic fat accumulation. Adapted from ref. 13, with permission from SNCSC. Here, we build on this model and demonstrate that Cotadutide improves whole-body insulin sensitivity through multimodal effects. In the liver, GCCR agonism enhances

insulin-stimulated signaling and improves hepatic insulin sensitivity. Cotadutide treatment also increases insulin-stimulated glucose uptake in the brown adipose tissue and enhances brown adipose tissue metabolic activity. These effects facilitate a reduced demand for insulin production in the pancreas and allow for recovery of endogenous β -cell function.

vehicle-treated mouse liver provide some molecular mechanistic insight into the cotadutide-induced improvement in hepatic insulin sensitivity demonstrated in the clamp studies.

Earlier studies demonstrated that cotadutide increased energy expenditure and reduced respiratory exchange ratio (RER) in DIO mice¹⁷ as well as increased lipid oxidation in hepatocytes¹³. In the current study, we show that cotadutide also has a robust, reproducible effect to specifically increase BAT glucose uptake associated with increased mitochondrial number and activity. This effect is predominantly driven by therapeutic GCCR agonism, since the same effect was strongly induced in mice treated with g1437 yet comparatively modest in mice treated with liraglutide. There have been a number of reports demonstrating glucagon-induced increases in energy expenditure in rodents^{23,64}, with some demonstrating BAT thermogenic activation^{65,66}. The mechanisms for glucagon-induced BAT activation are likely not a direct effect of glucagon action at adipocytes. While some have shown that glucagon may have a role for lipid metabolism in epicardial adipose tissue (EAT)⁶⁷, considering that the *Gcgr* is expressed much lower in adipose tissue relative to *Gcgr* expression in the liver⁶⁸, and with immunochemistry analysis indicating the GCCR to be

internalized in the cytosolic compartment⁶⁷, the physiological relevance of GCCR in white adipose tissue remains questionable. Indeed, for BAT, the GCCR protein is essentially not expressed, although mRNA expression data showed ~10,000-fold lower *Gcgr* expression in BAT than liver⁶⁴. Furthermore, no effect of BAT-specific GCCR KO was reported in a comprehensive metabolic phenotyping study in which response to exogenous glucagon was intact, with normal increase in energy expenditure as well as normal response to cold exposure⁶⁴. Glucagon agonism is known to stimulate FGF21 expression in the liver and raise circulating levels²¹. FGF21 is also known to stimulate adipose tissue activation through central and direct mechanisms^{69–72}. One study reported a partial reduction in glucagon-induced energy expenditure in FGF21 KO mice, suggesting there may be a contributory role for FGF21 in cotadutide-induced BAT activation. Indeed, we observed an increase in *Fgf21* gene expression in the liver and a trend toward elevated circulating FGF21 in cotadutide-treated mice. However, we cannot yet rule out other glucagon-induced hepatic derived factors may also contribute to the specific increase in BAT metabolic activity caused by cotadutide treatment. Evidence for the presence of BAT in adult humans⁷³ and functional significance in energy metabolism⁷⁴ is

growing, but its relevance for therapeutic targeting has yet to be demonstrated. Whether glucagon-induced energy expenditure, and BAT activation in particular, is relevant for adult humans remains an open question, but may have therapeutic benefit for some elements in the metabolic syndrome. Some human studies show increased glucagon-induced energy expenditure^{75–77}, although this could be independent of BAT activity⁷⁷, while others show no effect at all in individuals with obesity⁷⁸. Future clinical trials in GLP-1R/GCGR dual-agonists should assess circulating FGF21 and energy expenditure to better understand the mechanisms of action.

The cotadutide-induced improvement in insulin sensitivity consequently reduced the demand on pancreatic β -cells to secrete high levels of insulin to achieve physiological glucose uptake in peripheral tissues and suppress hepatic glucose production. The reduced demand for excess insulin secretion allowed for β -cell rest and functional recovery¹⁰. These results suggest a contrast to the known acute action of GLP-1 at the β -cell to increase glucose-stimulated insulin secretion and proinsulin synthesis²⁶, but do not contradict this expected effect. We have previously reported a cotadutide-induced increase of insulin secretion when a single dose was administered 60 min prior to a glucose tolerance test (GTT) in mice¹⁷. Similarly, following 6 weeks of daily injections, glucose-induced insulin secretion was potentiated when a dose of cotadutide was administered 240 min prior to the GTT¹³. Here, our studies were also performed following sub-chronic dosing of cotadutide, but outcome measures were timed to be in the absence of active compound (≥ 16 h after the final dose), so as to elucidate the lasting metabolic benefits of cotadutide, rather than its acute actions. Whether these beneficial effects on the β -cell and insulin secretion translate to humans has yet to be fully elucidated, but there are some hints emerging. In a renal impairment study of T2D patients that are dependent on insulin injection, cotadutide treatment decreased the required insulin dose by an average of 35.2% which is equivalent to 0.3 unit/kg reduction in insulin requirement, strongly suggesting improvement in insulin sensitivity in these patients¹⁹. In another study, peak insulin secretion was delayed following 49 days of daily cotadutide treatment, likely due to delayed gastric emptying²⁰. It is likely that these benefits are driven by a combination of GLP-1 and glucagon action, given their individual effects to reduce body weight, via reduced food intake, and liver fat content, respectively.

It is well appreciated that accumulation of ectopic fat, especially in the liver, can lead to an insulin-resistant state predominantly mediated by negative-feedback interference on insulin signal transduction pathways^{79,80}. Moreover, it is argued that the degree of hepatic insulin resistance can influence peripheral/whole-body insulin resistance^{81,82}. As such, if hepatic insulin resistance can be alleviated, improvements in peripheral insulin sensitivity will follow. Here we demonstrate, that activation of hepatic glucagon signaling in the context of a balanced GLP-1R/GCGR dual agonism therapeutic approach can dissipate liver ectopic fat (hepatic steatosis) that in turn rescues insulin sensitivity. This is predominately mediated by alleviation of negative feedback influence on hepatic insulin signal transduction pathways (Fig. 4). It also has the consequence of a specific metabolic activation of BAT to increase or sustain energy expenditure in the face of decreased food intake to “burn off” mobilized adipose tissue, that in part aids the reduction in hepatic steatosis. A second important consequence of recovering insulin sensitivity is to markedly reduce the insulin secretory demand on pancreatic β -cells and, via successive β -cell rest, restore normal endogenous β -cell function^{10,83} (Fig. 8). This then essentially reverses symptoms of T2D. Thus, this study supports the notion that GLP-1R/GCGR dual agonism might even be used as an early intervention in prediabetic patients, particularly those with elevated liver fat content, to reverse the prediabetic state and prevent the progression to T2D. This approach would then also protect the patient from other life-threatening co-morbidities associated with obesity and T2D, and have a major impact on the health care system.

A limitation to the hyperinsulinemic euglycemic clamp technique is that, despite infusion of equal concentration and rate of exogenous insulin to induce hyperinsulinemia, one cannot control endogenous insulin secretion, resulting in disparate levels of total circulating insulin during fasting and clamp periods between treatment groups. The use of somatostatin has been reported to block endogenous secretion of insulin and glucagon, however this technique cannot control for fasting levels and often introduces more variation and complicates interpretation. Therefore, current data is interpreted within the context of the measured circulating insulin concentration. Furthermore, in this experiment, it is difficult to compare the therapeutic effect of cotadutide, liraglutide, and g1437 with regard to the metabolic outcomes because the selected doses resulted in different magnitudes of weight loss. The doses were chosen with the goal of understanding the individual contributions of GLP-1R and GCGR agonism, and subsequent experiments adjusted doses to equalize weight loss between groups.

Phosphoproteomics provides a comprehensive view of cotadutide-induced changes in the proteome, as well as insulin-stimulated phosphoproteome; however, it will not detect all proteins and peptides within a sample. Therefore, some key proteins and peptides known to be involved in the insulin signaling pathway were not all identified. We addressed this, in part, through western blot and qPCR analysis of some known protein expression and phosphorylation sites. On the other hand, this study has identified previously unknown phosphorylation and dephosphorylation sites on several insulin signaling pathway elements. Because of the correlative improvement in hepatic insulin sensitivity observed, it is tempting to state that these represent phosphorylation sites associated with net positive effects of downstream insulin signal transduction. However, although that might be, it cannot be ruled out that some of these protein phosphorylation events may be neutral or even have a negative feedback effect to dampen insulin signaling. Further, molecular studies will be needed to confirm the function of these protein phosphorylation modifications. Finally, we note the limitations of our *in vivo* model system, including all murine studies being performed in male mice at 18–20 weeks of age. This approach is standard for the field, given that male mice present with metabolic disease more severely than females and that mice at this age develop the appropriate phenotype and reduce the burden of aging mice beyond this point⁸⁴. However, these factors do limit the studies transability to humans, given the associated discrepancies in disease presentation relating to gender and age.

Methods

Ethics statement

All studies were approved by the Institutional Animal Care and Use Committee at AstraZeneca or Vanderbilt University in accordance with the Animal Welfare Act guidelines.

Animal studies

Mice were housed in standard caging at 22 °C or 25 °C for PET studies, on a 12 h light:dark cycle with *ad libitum* access to food and water. All studies were performed in diet-induced obese C57Bl6J (Jackson Laboratories) male mice fed a 60% high-fat diet (D12492, Research Diets) for 8–12 weeks prior to study start and maintained for the study duration. Sex was considered in the study design and analysis. All murine studies were performed in male mice, as is standard in the field, because male mice present with metabolic disease more severely than females, and at the age utilized in the study, present the appropriate phenotype and reduce the burden of aging mice beyond this point.

Hyperinsulinemic euglycemic clamp and tissue-specific glucose uptake

C57Bl/6J diet-induced obese male mice were obtained from Jackson Laboratories at 20 weeks of age ($n = 7–11$). Mice underwent daily dosing of either vehicle, cotadutide (10 nmol/kg), liraglutide (5 nmol/kg),

or g1437 (5 nmol/kg) for 28 days. Catheters were implanted into a carotid artery for sampling, and a jugular vein for infusions, 7 days prior to the clamp. Mice were anesthetized with sodium pentobarbital, and the carotid artery and jugular vein were catheterized. Free catheter ends were tunneled under the skin to the back of the neck, externalized, and sealed with steel plugs. Lines were flushed daily with ~50 μ l saline containing 200 units/ml heparin and 5 mg/ml ampicillin. These methods permit arterial sampling from an indwelling catheter and are less stressful than cut-tail sampling⁸⁵. We fasted mice for 5 h and performed insulin clamps using a modified method from ref. 86. Essentially, the infusion, sampling, and calculation of glucose flux kinetics using [3-³H]-glucose during the clamp was as conducted as reported⁸⁷. Briefly, we primed [3-³H]-glucose (1.5 μ Ci) and then used a continuous infusion for 90 minutes as equilibration and basal sampling periods (0.075 μ Ci/min). After this, we mixed [3-³H]-glucose with the non-radioactive glucose infusate (infusate specific activity of 0.5 μ Ci/mg) during the 2-h clamp period. We clamped arterial glucose using a variable rate of glucose (plus trace [3-³H]-glucose) infusion, this was adjusted using blood glucose measurements collected at 10 min intervals. Mixing radioactive glucose with the non-radioactive glucose infused during clamping allows for deviations in arterial glucose specific activity to be minimized and steady-state conditions achieved, making calculation of glucose kinetics more robust⁸⁸. The mean values of blood samples collected at timepoints -15 and -5 min were used to calculate baseline blood or plasma variables. Insulin infusion (4 mU/kg body weight/min) was started at time point 0 and continued for 120 min. To prevent a fall in hematocrit, mice received heparinized saline-washed erythrocytes from donors at 5 μ l/min. Blood was collected from 80–120 min to determine [3-³H]-glucose. Clamp insulin was determined at timepoints 100 and 120 min. At 120 min, we administered 13 μ Ci of 2-[¹⁴C]deoxyglucose ([¹⁴C]2DG) to mice as an intravenous bolus. Blood was collected from 2–25 min to determine [¹⁴C]2DG. Finally, at the end of the study, mice were anesthetized and tissues were freeze-clamped for further ex vivo analysis. We determined plasma insulin levels using RIA and employed liquid scintillation counting to determine radioactivity of [3-³H]-glucose and [¹⁴C]2DG in the collected plasma samples and [¹⁴C]2DG-6-phosphate in the freeze-clamped tissues. Rates of glucose appearance (Ra) and disappearance (Rd) were calculated by steady-state equations as outlined⁸⁹. By subtracting the GIR from total Ra, the endogenous glucose appearance (endoRa) could be determined, and the glucose metabolic index (Rg) calculated using glucose metabolic rate per unit mass equations⁹⁰.

Hyperglycemic clamp and stable-isotope infusions

Twenty-week old C57Bl/6J DIO male mice (Jackson Laboratories) were dosed (-5 pm) with vehicle or cotadutide (10 nmol/kg), liraglutide (10 nmol/kg), or g1437 (10 nmol/kg) 2 h prior to lights out for 7 consecutive days ($n = 8$ –10). Hyperglycemic clamps were conducted as exactly reported¹³. Briefly, arterial and venous catheterization was conducted on mice five days prior to the clamp. Animals were 5-h fasted (starting at 7 am) on day 8 of the study. After 3 h of fasting on day 8, an arterial blood sample was collected to determine natural isotopic enrichment of plasma glucose. Immediately after collecting this sample, we conducted a quantitative stable isotope delivery to increase isotopic enrichment above natural isotopic labeling⁹¹. A [6,6-²H₂]Glucose-²H₂O (99.9%)-saline bolus was infused for 25 min to enrich total body water to 4.5% and provide a glucose prime (80 mg kg⁻¹) at timepoints -120 and -95 min. Following the 6,6-²H₂]Glucose-²H₂O-saline prime, a continuous infusion of [6,6-²H₂]glucose from time point -95 to 0 min (0.8 mg kg⁻¹ min⁻¹) was started. We initiated the hyperglycemic clamp at time point 0 min with a variable infusion of glucose ((50% dextrose + ²H₂O (0.04 MPE) + [6,6-²H₂]Glucose (0.08 MPE)), to induce stable hyperglycemia (250–300 mg/dL) and stable enrichment of ²H₂O and [6,6-²H₂]Glucose in plasma. Every 10 min, we observed the arterial glucose levels to inform adjustment of

the glucose infusion rate (GIR). We performed steady-state blood sampling for glucose kinetics at timepoints -10 and +90–120 min of hyperglycemia. Red blood cells were continuously infused during the hyperglycemic period to maintain hematocrit. At the end of study at time point 120 min, mice were anesthetized, sacrificed, and liver tissue was immediately frozen in liquid nitrogen. Stable isotopes were purchased from Cambridge Isotope Laboratories, Inc. (Tewksbury, MA). Each infusate was prepared in a 4.5% ²H₂O-enriched saline solution.

We employed GC-MS to determine plasma glucose enrichments ([6,6-²H₂]Glucose), isotopomer distribution and the enrichment ratio of deuterium on the fifth (C5) and second carbon (C2) of glucose^{92,93}. All plasma samples were chemically derivatized to obtain di-O-isopropylidene propionate, aldonitrile pentapropionate, and methyloxime pentapropionate derivatives of glucose.

Finally, liver glycogen was digested by amyloglucosidase⁹⁴ and glucose mass and enrichments were assessed in the homogenate in the same manner. To determine ²H₂O in plasma, the sample was spiked with [U-¹³C]acetone and NaOH. After exchange, we employed GC-MS and assayed ²H-enriched [U-¹³C]acetone following extraction with chloroform⁹⁵. Hepatic palmitate and glyceride enrichments and content were assessed in saponified extracts spiked with internal standards (1,1,2,3,3-²H₅Glycerol and Heptadecanoic acid)^{96,97}. Glucose fluxes were assessed using non-steady-state equations (volume of distribution of glucose = 130 ml/kg)⁸⁹. To determine the contributions of gluconeogenesis, we used the ratio of C5 and C2 of plasma glucose based on previous reports^{98,99}. We then calculated direct hepatic glycogen synthesis (6,6-²H₂]Glucose in glycogen = liver glycogen mass (mg/g) \times (glycogen [6,6-²H₂]Glucose MPE/ plasma [6,6-²H₂]Glucose MPE) from plasma glucose and percent indirect hepatic glycogen synthesis (C5/C2 in liver glycogen \times 100) from gluconeogenesis. At the same time we determined hepatic de novo lipogenesis and triglyceride esterification rates using the incorporation of ²H in palmitate and glyceride determines, respectively. Finally, the contribution of newly synthesized palmitate and esterified glycerol was determined using the following equations:

%newly made palmitate = Palmitate M + 1 MPE/(plasma ²H₂O MPE \times n) \times 100, where “ n ” represents the number of exchangeable hydrogens, which was assumed to be 22⁹⁶.

% newly made esterified glycerol = (Glycerol M + 1 enrichment MPE + 2 \times M + 2 enrichment MPE)/(plasma ²H₂O MPE \times 4.25) \times 100, where “ n ” represents the number of exchangeable hydrogens, which was assumed to be 4.25⁹⁶.

Insulin signaling and β -cell function studies

Male DIO C57Bl/6J mice at ~20 weeks of age were randomized to receive either vehicle or cotadutide (10 nmol/kg) daily for 28 days ($n = 8$). Cohort 1: On the morning following the final dose, mice were fasted for 5 h and administered either PBS or insulin (Humulin R; 0.75 U/kg). After 15 min, mice were sacrificed, and liver tissue was quickly dissected and frozen in liquid nitrogen for later phosphoproteomic analysis. The pancreas was collected and fixed in 10% formalin. Cohort 2: Mice were sacrificed on the morning following the final dose and whole pancreas was dissected, weighed and stored in 1.5% HCl in 70% ethanol for later measurement of total insulin content through acid-ethanol extraction and insulin ELISA (MSD Cat # K152BZC-2, Rockville, MD). Liver, white adipose, and brown adipose tissue pieces were also frozen in liquid nitrogen or stored for histological and electron microscopy analysis. Cohort 3: Mice were sacrificed on the morning following the final dose and pancreatic islets were isolated by collagenase digestion¹⁰⁰. Islets were then used for perfusion experiments or stored for electron microscopy analysis.

Islet perfusion

About 100 islets per pancreas of 75–125- μ m diameter were placed into individual perfusion columns in a 12-channel perfusion apparatus

(Biorep Technologies, Miami Lakers, FL). Islets underwent basal perfusion incubation for 90 min in 2.8 mmol/L glucose Krebs-Ringer bicarbonate HEPES buffer (KRBH). Biphasic insulin secretion was then assessed with the perfusion of 16.7 mmol/L glucose KRBH. Perfusate was collected from individual chambers at 2 min intervals and maintained at 4 °C, and insulin concentrations were determined using insulin ELISA (MSD). Islets protein content was assessed following the experiment for normalization.

Liver phosphoproteomics

For each condition, $n = 4$ mice per group was analyzed for a total of 16 samples. Each sample was homogenized on ice in 6 M urea, 2 M Thiourea, 10 mM DTT, cOmplete Protease Inhibitor and phosphatases inhibitor cocktail (PhosSTOP) using a probe sonicator 3×20 s at 60% amplitude. After sonication, the samples were centrifuged at $14,000 \times g$ for 20 min at 4 °C. The supernatant was recovered, and the protein concentration was measured using a Nanodrop. A total of 300 μ g of protein was taken out, and 20 mM Iodoacetamide was added, and the samples were incubated for 30 min at RT in the dark. After incubation, the proteins were precipitated using ice-cold Ethanol/Acetone precipitation. The precipitated protein was resolubilized in 5% sodium deoxycholate (SDC) in 50 mM HEPES buffer, pH 8.5. The proteins were digested with 5% modified Trypsin and 0.4 μ g endoproteinase Lys-C overnight at 37 °C. After digestion, 100 μ g was taken out for each sample for TMTpro labeling according to the manufacturer's protocol. The samples were labeled accordingly: Vehicle plus PBS (TMT126-128N); Cotadutide plus PBS (TMT128C-130N); Vehicle plus Insulin (TMT130C-132N); Cotadutide plus Insulin (TMT132C-134N). After labeling, the samples were mixed and 1 M Ammonium bicarbonate was added to 10 mM for 15 min in order to block remaining TMT. The SDC was precipitated by acidification to 2% formic acid, followed by centrifugation to recover the supernatant. The recovered TMT-labeled peptides were lyophilized for further purification of phosphopeptides.

Enrichment of phosphopeptides

The purification of phosphorylated peptides was performed using titanium dioxide (TiO_2) chromatography described in detail below. To ensure high enrichment efficiency and to eliminate co-purified sialic acid-containing N-linked glycopeptides the phosphopeptides were purified using a double TiO_2 enrichment strategy with an enzymatic de-glycosylation step between the TiO_2 enrichment steps. The final phosphopeptide sample was fractionated using high-pH reversed-phase (HpH RP) separation prior to LC-MS/MS. The lyophilized TMT-labeled peptides were resuspended in TiO_2 loading buffer (80% acetonitrile (ACN), 5% trifluoroacetic acid (TFA), 1 M glycolic acid) and incubated with 0.6 mg TiO_2 beads (GL Science, Japan) per 100 μ g peptide on a shaker for 10 min. After incubation and centrifugation, the supernatant was incubated again with 0.3 mg TiO_2 beads per 100 μ g on a shaker for 10 min. After incubation, all TiO_2 beads were sequentially washed together in one tube with 100 μ L 80% ACN, 1% TFA, and subsequently with 20% ACN, 0.1% TFA. All supernatants from the washes were collected, lyophilized, and stored for desalting by HLB reversed-phase chromatography. The TiO_2 beads were dried, and subsequently resolubilized in 150 μ L 100 mM HEPES buffer, pH 8, containing 1 μ L PNGaseF (0.5 U) (New England BioLabs) to remove the sialylated N-linked glycan structures from the enriched sialic acid-containing N-linked glycopeptides that are co-enriched in the TiO_2 . The sample was incubated at 37 °C overnight. After incubation, the sample was diluted to 80% ACN, 1% TFA and incubated on a shaker at RT for 10 min, to allow the phosphopeptides to re-attach to the TiO_2 beads. After incubation, the beads were pelleted by centrifugation, and the supernatant, containing the deglycopeptides, was removed, and the TiO_2 beads were washed with 200 μ L 50% ACN, 0.1% TFA. The beads were pelleted, and the supernatant was recovered with the other supernatant. The

TiO_2 beads were dried, and the bound phosphopeptides were eluted from the beads with 1% ammonium hydroxide solution, pH 11.3, as described above. The phosphopeptides were lyophilized prior to HpH RP separation.

Desalting of the “non-modified peptide” fraction using HLB RP Chromatography

The lyophilized flow-through from TiO_2 chromatography was resuspended in 2 ml 0.1% TFA. An Oasis HLB cartridge (Waters.com) was washed with 2 mL of MeOH and ACN, respectively, and equilibrated using 3 mL 0.1% TFA. The peptide sample was loaded slowly onto the cartridge using a 10 mL Syringe. After loading, the cartridge was washed using 3 mL 0.1% TFA. The peptides were recovered using 1 mL 60% ACN/ H_2O into a low-binding tube and lyophilized prior to High-pH RP fractionation.

High-pH reversed-phase fractionation

The phosphorylated peptides and “non-modified” peptides were re-dissolved in 35 μ L 20 mM ammonium formate, pH 9.3 and sonicated for 5 min. The samples were centrifuged for 15 min at $14,000 \times g$ at room temperature, and the supernatant was applied to an ACQUITY UPLC M-class CSH C18, 1.7 μ m 300 μ m \times 100 mm RP column using a Dionex 3000 Ultimate system. The peptides were eluted from the C18 column with increasing concentrations of acetonitrile in ammonium formate (2, 50, 95% acetonitrile) for 155 min with a flow rate of 5.0 μ L/min. The samples were fractionated into 20 concatenated fractions. The fractions were lyophilized prior to LC-MS/MS.

Liquid chromatography tandem mass spectrometry (LC-MS/MS) –phosphoproteomics

The various samples were analyzed on an EASY nanoLC system coupled with a Fusion Lumos Tribrid (“non-modified peptides”) or an Orbitrap Eclipse Tribrid (phosphopeptides). Lyophilized peptides from the HpH RP fractionation (20 concatenated fractions) were resolubilized in 3–5 μ L of 0.1% formic acid (FA) and loaded onto a 20 cm analytical column (100- μ m inner diameter) packed with ReproSil–Pur C18 AQ 1.9 μ m reversed-phase material. The peptides were eluted with an organic solvent gradient from 100% phase A (0.1% FA) to 25% phase B (95% ACN, 0.1% FA) for 100 min, then from 25% B to 40% B for 20 min before the column was washed with 95% B. The flow rate was set to 300 nL/min during elution. For the two instruments, the automatic gain control target value of 1.5×10^6 ions in MS and a maximum fill time of 50 ms was used. Each MS scan was acquired at high resolution (120,000 full width half maximum (FWHM)) at m/z 200 in the Orbitrap with a mass range of 350–1400/1500 Da. The instruments were set to select as many precursor ions as possible in 3 s between the MS analyses. Peptide ions were selected from the MS for higher energy collision-induced dissociation (HCD) fragmentation (collision energy: 34%). Fragment ions were detected in the orbitrap at high resolution (50,000 FWHM) for a target value of 1.5×10^5 ions and a maximum injection time of 200 ms (phosphopeptides) or 86 ms (“non-modified peptides”) using an isolation window of 0.7 Da and a dynamic exclusion of 20–30 s. All raw data were viewed in Xcalibur v3.0 (Thermo Fisher Scientific).

Peptide/protein identification and quantitation

All LC-MS/MS raw data files were searched using Proteome Discoverer (PD) version 2.5.0.400 (Thermo Fisher Scientific). The raw data were searched in PD using a workflow where the raw data were first subjected to database searching using an in-house Mascot server (Version 2.2.04, Matrix Science Ltd., London, UK). The searches had the following criteria: database, SwissProt mouse protein database; enzyme, trypsin; maximum missed cleavages, 2; fixed modifications, TMTpro (N-terminal), TMTpro (K), and Carbamidomethyl (C). Variable modification for the phosphopeptides was phospho (S/T/Y) and

deamidation (N), whereas no variable modifications were used for the “non-modified peptides”. The peptide fragment ion spectra that were not identified as a peptide in Mascot with a below 1% false discovery rate (FDR) was further subjected to database searching using SEQUEST HT in PD. The database used here was a UniProt mouse protein database (April 2023). The searching criteria was as described for the Mascot search. Peptides were accepted for further analysis if they had a q value below 0.01 (Percolator)^{101,102}, corresponding to 1% FRD, had Mascot rank 1, and a cut-off value of Mascot score $>18^{103}$. The TMT16 plex reporter ion signals were quantified using S/N, and they were normalized to the total peptide S/N in the PD program. The in-built ANOVA test in PD was used to generate p values for all the phosphopeptides and proteins identified in the database searches. KEGG enrichment analysis was performed with STRING.

PET study

[18F]FDG-PET imaging was performed on days 0, 14, and 28. On the days of imaging mice were fasted for 4 h and then intravenously (tail vein) administered with [18F]FDG (~200 uCi). Mice were anesthetized using isoflurane/O₂ (1.5 to 3% v/v) and imaged (nanoScan PET/CT) at 1 h post [18F] FDG injection. During the course of imaging (20 min), mice received isoflurane/O₂ and were maintained at 37 °C by the heated bed on the scanner. At the end of the study, mice were euthanized (CO₂ asphyxiation), and necropsy was performed to obtain tissues/organs from each mouse. Radioactivity associated with each sample was determined by gamma counting (PerkinElmer Wizard2). PET/CT images were analyzed using VivoQuant software. PET/CT and gamma counter data were plotted using GraphPad Prism.

Immunohistochemistry and β -cell and α -cell mass analysis

Pancreata, BAT, and liver were fixed in 10% formalin for 24 h and paraffin-embedded. Pancreata were sliced at 5- μ m sections and three sections per pancreas separated by 50 μ m were used for multiplex staining of insulin (#ab181547, Abcam), glucagon (#2760 Cell Signaling Technology), and MafA (#IHC-00352, Bethyl Labs, Montgomery, TX), followed by Mayer's hematoxylin (Dako). BAT was sectioned and immuno-stained for UCP-1 (#ab23841, Abcam). Immunohistochemistry was performed using a Ventana Discovery ULTRA Staining Module (Ventana Medical System; Glucagon and insulin) or a Leica Bond RX Autostainer (Leica Microsystems, Inc., Buffalo Grove, IL; Mafa and UCP-1). For H&E, liver and BAT slides were first incubated in Mayer's hematoxylin (Dako), washed in tap water, and stained with eosin Y solution (Sigma) before being hydrated and mounted using Pertex.

Histological analysis

All tissues/organs were examined for histopathological changes, which were diagnosed following the International Harmonization of Nomenclature and Diagnostic Criteria (INHAND), Society of Toxicological Pathology (www.toxpath.org/inhand.asp). Microvesicular score for brown adipose tissue H&E were graded semi-quantitatively using a score from 1 to 5¹⁰⁴. In the multiple IHC-stained pancreata slides, the stained area and the total section area was detected by threshold and machine learning in the Visiopharm image analysis system. The insulin and glucagon positive area was quantified and expressed as β -cell and α -cell mass calculated by β - or α -cell area: pancreas area \times pancreas weight. Mafa staining was expressed as Mafa + nuclei per mm² tissue. For liver H&E slides, an Artificial Intelligence (AI) application was used to detect and count hepatic fat droplets in the Visiopharm image analysis system. The hepatic fat-areas were initially manually annotated on a high number of sections, thereby teaching the machine learning algorithm how to distinguish these two areas, hepatic cells with single droplets (macrovesicular) and hepatocytes included multiple small droplets (microvesicular), from background such as vessels and artefacts. To avoid including glycogen, only circular droplets inside the hepatocytes were used to assess hepatic

lipid fractional area, and to count the number of hepatocytes including lipid droplets.

Electron microscopy for isolated islets and BAT

Freshly isolated islets or BAT cut to ~2 mm \times 1 mm \times 1 mm pieces were fixed in 0.1 mol/L cacodylate buffer with 4% paraformaldehyde and 2% glutaraldehyde. Samples were embedded in resin and subsequently sectioned and stained. Imaging was conducted using a Thermo/FEI Tecnai F30 300 kV 3D electron tomography/ STEM tomography instrument. Islet images were analyzed for the number of mature and immature islets per cytoplasmic area from 29 to 31 electron micrographs per group. BAT images were analyzed for lipid droplet and mitochondrial area. Quantification of organelle size/area in electron micrographs was conducted by tracing organelles, and their cell surface area/total cell area calculated¹⁰⁵.

RNA isolation from adipose tissue

RNA was isolated from 30 mg of BAT and 100 mg of WAT tissue. Samples were homogenized in 800- μ l trizol, incubated for 5 min, and the fat layer was removed. An additional 200 μ l of trizol was added to the homogenate, followed by 200 μ l 1-bromo-3-chloropropane (BCP). Samples were mixed, incubated at room temperature for 10 min, and centrifuged at 12,000 $\times g$ for 14 min at 4 °C. The aqueous phase was transferred to a new tube, and 600 μ l of 70% ethanol added. Samples were then transferred to an RNeasy Mini spin column, centrifuged at 10,000 $\times g$ for 15 s followed by 700 μ l Buffer RW1 and centrifuged. Eighty μ l of DNase was added to the column and incubated at RT for 15 min, followed by 500 μ l RPE and centrifuged. RPE wash was performed a second time, and the spin column was placed in a new tube. Thirty μ l of water was applied to the column and centrifuged at 10,000 $\times g$ for 1 min to elute the RNA. RNA-seq libraries were generated and sequenced at GENEWIZ, and data analyzed at AstraZeneca.

Library preparation with polyA selection and HiSeq sequencing

RNA library preparations and sequencing reactions were conducted at GENEWIZ, LLC. (South Plainfield, NJ, USA). RNA samples received were quantified using Qubit 2.0 Fluorometer (Life Technologies, Carlsbad, CA, USA), and RNA integrity was checked using Agilent TapeStation 4200 (Agilent Technologies, Palo Alto, CA, USA). RNA sequencing libraries were prepared using the NEBNext Ultra RNA Library Prep Kit for Illumina following the manufacturer's instructions (NEB, Ipswich, MA, USA). Briefly, mRNAs were first enriched with Oligo(dT) beads. Enriched mRNAs were fragmented for 15 min at 94 °C. First strand and second strand cDNAs were subsequently synthesized. cDNA fragments were end repaired and adenylated at 3'ends, and universal adapters were ligated to cDNA fragments, followed by index addition and library enrichment by limited-cycle PCR. The sequencing libraries were validated on the Agilent TapeStation (Agilent Technologies, Palo Alto, CA, USA), and quantified by using Qubit 2.0 Fluorometer (Invitrogen, Carlsbad, CA) as well as by quantitative PCR (KAPA Biosystems, Wilmington, MA, USA). The sequencing libraries were clustered on two lanes of a flowcell. After clustering, the flowcell was loaded on the Illumina HiSeq instrument (4000 or equivalent) according to the manufacturer's instructions. The samples were sequenced using a 2 \times 150bp paired-end (PE) configuration. Image analysis and base calling were conducted by the HiSeq Control Software (HCS). Raw sequence data (.bcl files) generated from Illumina HiSeq was converted into fastq files and de-multiplexed using Illumina's bcl2fastq 2.17 software. One mismatch was allowed for index sequence identification.

RNA-seq data analysis

Adapter sequences were removed using Trimmomatic v.0.36¹⁰⁶. Short sequencing reads were mapped to the mouse genome (mm10) using STAR v.2.5.2b¹⁰⁷. Read counts were calculated using featureCounts from Subread v.1.5.2¹⁰⁸. Differential expression analysis was performed

with DESeq2¹⁰⁹. Genes with Benjamini–Hochberg false discovery rate <0.05 were considered significant. Gene Ontology^{110,111} enrichment analysis was performed with AmiGO¹¹².

RNA isolation from murine liver and qRT-PCR

For RNA isolation of murine liver tissue, 10 mg sample were homogenized in buffer RLT using Lysing Matrix D tubes (Millipore, Ref #116913050). Homogenates were centrifuged at max speed (15,000 × g) for 10 min, and supernatant was removed using a syringe to avoid fats. Centrifugations were repeated for a total of three spins to clear sufficient fat from the samples. RNA was then isolated using a RNeasy Kit (QIAGEN, Ref # 74104). Equal amounts of RNA were reverse transcribed to complementary DNA using a high-capacity RNA-to-DNA kit (Invitrogen, Ref #18080400) according to the manufacturer's directions. For quantitative real-time PCR, a QuantStudio-7 Flex System was used and TaqMan Standard PCR Master Mix and TaqMan probes were employed. Each sample was tested in triplicate and quantified using the $2^{-\Delta\Delta C_t}$ method to calculate the relative gene expression relative to endogenous control *Rps14*.

ELISA from murine plasma

Plasma samples were stored at −80 °C until use, with freeze-thaws kept to a minimum. ELISA was run using Mouse/Rat Fgf21 Quantikine ELISA Kit (R&D Systems, Ref #MF2100) following the manufacturer's instructions. Briefly, 50 µL of Assay Diluent RD1-41 was added to each well, followed by 50 µL of sample diluted in Calibrator Diluent RD6Z 3x prior to use, prepared control, or prepared standard, and covered and incubated at RT for 2 h. Wells were washed 5X with 370 µL Wash Buffer. To each well, 100 µL of Fgf21 conjugate was added and covered and incubated at RT for 2 h. Wells were washed 5X with 370 µL wash buffer. To each well, 100 µL freshly prepared substrate solution was added and incubated at RT for 30 min, followed by 100 µL Stop Solution. The optical density of each well was determined using a plate reader set to 450 with a correction at 540 nm.

Immunoblotting from murine liver tissue

For protein isolation of murine liver tissue, 10 mg sample were suspended in 300 µL cold RIPA lysis buffer (Thermo, Ref #89901) containing protease and phosphatase inhibitor (Thermo, Ref #1861280) in protein lysis tubes (Qiagen, Ref # 19560) containing one, 2.5-mm ceramic bead and one, 5-mm steel bead (Qiagen, Ref # 13114, and Ref #69989). Samples were lysed on a Qiagen TissueLyser II at a frequency of 27 for 5 min. Lysed samples were centrifuged at 15,000 × g for 20 min at 1 °C, and supernatant removed for immunoblotting using a syringe to avoid transfer of fats. Lysates were quantified using the Pierce BCA Protein Assay Kit (Pierce, Ref #23227). Approximately, 25 µg of protein was diluted in 4x NuPAGE buffer (Thermo, Ref # NP0007), 10x NuPAGE reducing agent (Ref #NP0004), and water to bring to a total volume of 20 µL. Samples were boiled at 70 °C for 10 min, then electrophoresed at −100 V for −1.5 h using the NuPAGE electrophoresis system employing a NuPAGE 4–12% Bis-Tris Gel, 1X NuPAGE MES SDS Running Buffer, and NuPAGE Antioxidant (Thermo, Ref #NP0322, #NP0002, and #NP0005, respectively). Protein samples were compared to Novex Pre-Stained Protein Standard and Magic Mark XP Western Protein Standard combined in a 1:1 dilution (Thermo, Ref # LC5800, #LC5602). Samples were dry transferred to nitrocellulose membrane using the IBlot 2 system and reagents (Thermo, Ref #IB21001, #IB23002). Membranes were blocked for 1 h in Licor Intercept Blocking Buffer (Ref #927-60001) and then incubated in primary antibodies for total Akt (Cell Signaling, Ref #9272S, 1:1000), phospho-Akt Serine 473 (Cell Signaling, Ref # 4060S, 1:1000), or phospho-Akt Threonine 308 (Cell Signaling, Ref #13038, 1:1000) diluted in Licor Intercept Protein-Free Antibody Diluent (Ref #927-85001) at 4 °C overnight. Membranes were washed in TBST 10 min, 3X, and then incubated in Licor Goat Anti-rabbit secondary antibodies diluted 1:20,000 in Licor Intercept Protein-Free Antibody

Diluent for 1 h. Membranes were washed in TBS 10 min, 3X and then imaged on a Licor Odyssey Imager.

Statistics

Data were expressed as means ± s.e.m. Unless indicated otherwise, such as for sequencing and mass-spec data, all statistical analyses were carried out using GraphPad Prism 9 (GraphPad Software, San Diego, CA). The data were analyzed via Student's *t*-test, one-way or two-way ANOVA with post hoc tests as indicated in the figure legends. Values of $p \leq 0.05$ were considered to represent statistically significant differences. Replicates represent distinct samples unless indicated otherwise in the figure legends.

Reporting summary

Further information on research design is available in the Nature Portfolio Reporting Summary linked to this article.

Data availability

RNA-seq datasets generated in this study have been deposited in the GEO database under accession code [GSE284233](https://www.ncbi.nlm.nih.gov/geo/query/acc.cgi?acc=GSE284233). The mass spectrometry proteomics data have been deposited to the ProteomeXchange Consortium via the PRIDE partner repository with the dataset identifier [PXD057744](https://www.ebi.ac.uk/pride/archive/study/PXD057744). All other raw data generated in this study are provided in the supplementary information or the Source Data file. Source data are provided with this paper.

Code availability

Custom codes are deposited on Zenodo as [Data Visualization Code for R](https://zenodo.org/records/13444444). There are no restrictions.

References

- Kosmalski, M. et al. The coexistence of nonalcoholic fatty liver disease and type 2 diabetes mellitus. *J Clin Med.* **11**, 1375 (2022).
- Chen, K. et al. Clinical spectrum of non-alcoholic fatty liver disease in patients with diabetes mellitus. *PLoS ONE* **15**, e0236977 (2020).
- Plantinga, L. C. et al. Prevalence of chronic kidney disease in US adults with undiagnosed diabetes or prediabetes. *Clin. J. Am. Soc. Nephrol.* **5**, 673–682 (2010).
- Xu, M. et al. Type 2 diabetes, diabetes genetic score and risk of decreased renal function and albuminuria: a Mendelian randomization study. *EBioMedicine* **6**, 162–170 (2016).
- Causy, C., Aubin, A. & Loomba, R. The relationship between type 2 diabetes, NAFLD, and cardiovascular risk. *Curr. Diab. Rep.* **21**, 15 (2021).
- Marín-Peñalver, J. J. et al. Update on the treatment of type 2 diabetes mellitus. *World J. Diabetes* **7**, 354–395 (2016).
- Nkonge, K. M., Nkonge, D. K. & Nkonge, T. N. Insulin therapy for the management of diabetes mellitus: a narrative review of innovative treatment strategies. *Diabetes Ther.* **14**, 1801–1831 (2023).
- Herman, W. H. et al. Early detection and treatment of type 2 diabetes reduce cardiovascular morbidity and mortality: a simulation of the results of the Anglo-Danish-Dutch study of intensive treatment in people with screen-detected diabetes in primary care (ADDITION-Europe). *Diabetes Care* **38**, 1449–1455 (2015).
- Narayan, K. M. & Gujral, U. P. Evidence tips the scale toward screening for hyperglycemia. *Diabetes Care* **38**, 1399–1401 (2015).
- Boland, B. B., Rhodes, C. J. & Grimsby, J. S. The dynamic plasticity of insulin production in β -cells. *Mol. Metab.* **6**, 958–973 (2017).
- Nahra, R. et al. Effects of cotadutide on metabolic and hepatic parameters in adults with overweight or obesity and type 2 diabetes: a 54-week randomized phase 2b study. *Diabetes Care* **44**, 1433–1442 (2021).
- Ambery, P. et al. MEDI0382, a GLP-1 and glucagon receptor dual agonist, in obese or overweight patients with type 2 diabetes: a

- randomised, controlled, double-blind, ascending dose and phase 2a study. *Lancet* **391**, 2607–2618 (2018).
13. Boland, M. L. et al. Resolution of NASH and hepatic fibrosis by the GLP-1R/GcgR dual-agonist Cotadutide via modulating mitochondrial function and lipogenesis. *Nat. Metab.* **2**, 413–431 (2020).
 14. Chung, S. M. et al. Long-term effects of the changes in hepatic steatosis status on the risk of incident type 2 diabetes mellitus: a 15-year community-based prospective cohort study. *Diabetes Res. Clin. Pr.* **184**, 109208 (2022).
 15. Nasr, P. et al. The amount of liver fat predicts mortality and development of type 2 diabetes in non-alcoholic fatty liver disease. *Liver Int.* **40**, 1069–1078 (2020).
 16. Targher, G. et al. The complex link between NAFLD and type 2 diabetes mellitus - mechanisms and treatments. *Nat. Rev. Gastroenterol. Hepatol.* **18**, 599–612 (2021).
 17. Henderson, S. J. et al. Robust anti-obesity and metabolic effects of a dual GLP-1/glucagon receptor peptide agonist in rodents and non-human primates. *Diabetes Obes. Metab.* **18**, 1176–1190 (2016).
 18. Ambery, P. D. et al. MEDI0382, a GLP-1/glucagon receptor dual agonist, meets safety and tolerability endpoints in a single-dose, healthy-subject, randomized, phase 1 study. *Br. J. Clin. Pharm.* **84**, 2325–2335 (2018).
 19. Parker, V. E. R. et al. Efficacy and safety of cotadutide, a dual glucagon-like peptide-1 and glucagon receptor agonist, in a randomized phase 2a study of patients with type 2 diabetes and chronic kidney disease. *Diabetes Obes. Metab.* **24**, 1630–1639 (2022).
 20. Parker, V. E. R. et al. Efficacy, safety, and mechanistic insights of cotadutide, a dual receptor glucagon-like peptide-1 and glucagon agonist. *J. Clin. Endocrinol. Metab.* **105**, dgz047 (2020).
 21. Habegger, K. M. et al. Fibroblast growth factor 21 mediates specific glucagon actions. *Diabetes* **62**, 1453–1463 (2013).
 22. Nason, S. R. et al. Glucagon receptor signaling regulates weight loss via central KLB receptor complexes. *JCI Insight* **6**, e141323 (2021).
 23. Kim, T. et al. Glucagon receptor signaling regulates energy metabolism via hepatic farnesoid X receptor and fibroblast growth factor 21. *Diabetes* **67**, 1773–1782 (2018).
 24. Novikoff, A. & Müller, T. D. The molecular pharmacology of glucagon agonists in diabetes and obesity. *Peptides* **165**, 171003 (2023).
 25. Boland, B. B. et al. β -cell control of insulin production during starvation-refeeding in male rats. *Endocrinology* **159**, 895–906 (2018).
 26. Alarcon, C., Wicksteed, B. & Rhodes, C. J. Exendin 4 controls insulin production in rat islet beta cells predominantly by potentiation of glucose-stimulated proinsulin biosynthesis at the translational level. *Diabetologia* **49**, 2920–2929 (2006).
 27. Humphrey, S. J. et al. Dynamic adipocyte phosphoproteome reveals that Akt directly regulates mTORC2. *Cell Metab.* **17**, 1009–1020 (2013).
 28. Saha, M. et al. RSK phosphorylates SOS1 creating 14-3-3-docking sites and negatively regulating MAPK activation. *Biochem. J.* **447**, 159–166 (2012).
 29. Baljuls, A. et al. Positive regulation of A-RAF by phosphorylation of isoform-specific hinge segment and identification of novel phosphorylation sites. *J. Biol. Chem.* **283**, 27239–27254 (2008).
 30. Maccario, H. et al. PTEN is destabilized by phosphorylation on Thr366. *Biochem. J.* **405**, 439–444 (2007).
 31. Vazquez, F. et al. Phosphorylation of the PTEN tail regulates protein stability and function. *Mol. Cell Biol.* **20**, 5010–5018 (2000).
 32. Parker, B. L. et al. Targeted phosphoproteomics of insulin signaling using data-independent acquisition mass spectrometry. *Sci. Signal* **8**, rs6 (2015).
 33. Huang, X. et al. The PI3K/AKT pathway in obesity and type 2 diabetes. *Int. J. Biol. Sci.* **14**, 1483–1496 (2018).
 34. Kim, T. et al. Hepatic mTORC2 signaling facilitates acute glucagon receptor enhancement of insulin-stimulated glucose homeostasis in mice. *Diabetes* **71**, 2123–2135 (2022).
 35. Kim, T. et al. Hepatic glucagon receptor signaling enhances insulin-stimulated glucose disposal in rodents. *Diabetes* **67**, 2157–2166 (2018).
 36. Besse-Patin, A. et al. PGC1A regulates the IRS1:IRS2 ratio during fasting to influence hepatic metabolism downstream of insulin. *Proc. Natl Acad. Sci. USA* **116**, 4285–4290 (2019).
 37. Habegger, K. M. Cross talk between insulin and glucagon receptor signaling in the hepatocyte. *Diabetes* **71**, 1842–1851 (2022).
 38. Luo, X. et al. Fasting-induced protein phosphatase 1 regulatory subunit contributes to postprandial blood glucose homeostasis via regulation of hepatic glycogenesis. *Diabetes* **60**, 1435–1445 (2011).
 39. Li, Q. et al. The protein phosphatase 1 complex is a direct target of AKT that links insulin signaling to hepatic glycogen deposition. *Cell Rep.* **28**, 3406–3422.e7 (2019).
 40. Ros, S. et al. Control of liver glycogen synthase activity and intracellular distribution by phosphorylation. *J. Biol. Chem.* **284**, 6370–6378 (2009).
 41. Zois, C. E. & Harris, A. L. Glycogen metabolism has a key role in the cancer microenvironment and provides new targets for cancer therapy. *J. Mol. Med.* **94**, 137–154 (2016).
 42. Zhang, H. H. et al. Insulin stimulates adipogenesis through the Akt-TSC2-mTORC1 pathway. *PLoS ONE* **4**, e6189 (2009).
 43. Ranek, M. J. et al. PKG1-modified TSC2 regulates mTORC1 activity to counter adverse cardiac stress. *Nature* **566**, 264–269 (2019).
 44. Gwinn, D. M. et al. AMPK phosphorylation of raptor mediates a metabolic checkpoint. *Mol. Cell* **30**, 214–226 (2008).
 45. Hong, S. et al. LARP1 functions as a molecular switch for mTORC1-mediated translation of an essential class of mRNAs. *Elife* **6**, e25237 (2017).
 46. Jia, J. J. et al. mTORC1 promotes TOP mRNA translation through site-specific phosphorylation of LARP1. *Nucleic Acids Res.* **49**, 3461–3489 (2021).
 47. Qin, X., Jiang, B. & Zhang, Y. 4E-BP1, a multifactor regulated multifunctional protein. *Cell Cycle* **15**, 781–786 (2016).
 48. Meyuhas, O. Ribosomal protein S6 phosphorylation: four decades of research. *Int. Rev. Cell Mol. Biol.* **320**, 41–73 (2015).
 49. Eguchi, J. et al. Transcriptional control of adipose lipid handling by IRF4. *Cell Metab.* **13**, 249–259 (2011).
 50. Kong, X. et al. IRF4 is a key thermogenic transcriptional partner of PGC-1 α . *Cell* **158**, 69–83 (2014).
 51. Gómez-Banoy, N. et al. Adipsin preserves beta cells in diabetic mice and associates with protection from type 2 diabetes in humans. *Nat. Med.* **25**, 1739–1747 (2019).
 52. Lo, J. C. et al. Adipsin is an adipokine that improves β cell function in diabetes. *Cell* **158**, 41–53 (2014).
 53. Carmona, M. C. et al. Mitochondrial biogenesis and thyroid status maturation in brown fat require CCAAT/enhancer-binding protein alpha. *J. Biol. Chem.* **277**, 21489–21498 (2002).
 54. Carmona, M. C. et al. Defective thermoregulation, impaired lipid metabolism, but preserved adrenergic induction of gene expression in brown fat of mice lacking C/EBPbeta. *Biochem. J.* **389**, 47–56 (2005).
 55. Wu, L. et al. Cidea controls lipid droplet fusion and lipid storage in brown and white adipose tissue. *Sci. China Life Sci.* **57**, 107–116 (2014).
 56. Parker, V. E. R. et al. Cotadutide promotes glycogenolysis in people with overweight or obesity diagnosed with type 2 diabetes. *Nat. Metab.* **5**, 2086–2093 (2023).
 57. Asano, M. et al. Pharmacokinetics, safety, tolerability and efficacy of cotadutide, a glucagon-like peptide-1 and glucagon receptor dual agonist, in phase 1 and 2 trials in overweight or obese

- participants of Asian descent with or without type 2 diabetes. *Diabetes Obes. Metab.* **23**, 1859–1867 (2021).
58. Shankar, S. S. et al. Safety and efficacy of novel incretin co-agonist cotadutide in biopsy-proven noncirrhotic MASH with fibrosis. *Clin. Gastroenterol. Hepatol.* **22**, 1847–1857.e11 (2024).
 59. Golubic, R. et al. Dual glucagon-like peptide-1 and glucagon receptor agonism reduces energy intake in type 2 diabetes with obesity. *Diabetes Obes. Metab.* **26**, 2634–2644 (2024).
 60. Klein, G. et al. Pharmacokinetics and safety of cotadutide, a GLP-1 and glucagon receptor dual agonist, in individuals with renal impairment: a single-dose, phase I, bridging study. *Clin. Pharmacokinet.* **62**, 881–890 (2023).
 61. Selvarajah, V. et al. A randomized phase 2b trial examined the effects of the glucagon-like peptide-1 and glucagon receptor agonist cotadutide on kidney outcomes in patients with diabetic kidney disease. *Kidney Int.* **106**, 1170–1180 (2024).
 62. Stagner, J. I. & Samols, E. The vascular order of islet cellular perfusion in the human pancreas. *Diabetes* **41**, 93–97 (1992).
 63. Alford, F. P., Bloom, S. R. & Nabarro, J. D. Glucagon metabolism in man, studies on the metabolic clearance rate and the plasma acute disappearance time of glucagon in normal and diabetic subjects. *J. Clin. Endocrinol. Metab.* **42**, 830–838 (1976).
 64. Beaudry, J. L. et al. The brown adipose tissue glucagon receptor is functional but not essential for control of energy homeostasis in mice. *Mol. Metab.* **22**, 37–48 (2019).
 65. Billington, C. J. et al. Glucagon in physiological concentrations stimulates brown fat thermogenesis in vivo. *Am. J. Physiol.* **261**, R501–R507 (1991).
 66. Kinoshita, K. et al. Glucagon is essential for adaptive thermogenesis in brown adipose tissue. *Endocrinology* **155**, 3484–3492 (2014).
 67. Malavazos, A. E. et al. Human epicardial adipose tissue expresses glucose-dependent insulinotropic polypeptide, glucagon, and glucagon-like peptide-1 receptors as potential targets of pleiotropic therapies. *Eur. J. Prev. Cardiol.* **30**, 680–693 (2023).
 68. Gao, C. et al. Glucagon receptor antagonist for heart failure with preserved ejection fraction. *Circ. Res.* **135**, 614–628 (2024).
 69. Owen, B. M. et al. FGF21 acts centrally to induce sympathetic nerve activity, energy expenditure, and weight loss. *Cell Metab.* **20**, 670–677 (2014).
 70. Xu, J. et al. Fibroblast growth factor 21 reverses hepatic steatosis, increases energy expenditure, and improves insulin sensitivity in diet-induced obese mice. *Diabetes* **58**, 250–259 (2009).
 71. Douris, N. et al. Central fibroblast growth factor 21 browns white fat via sympathetic action in male mice. *Endocrinology* **156**, 2470–2481 (2015).
 72. BonDurant, L. D. et al. FGF21 regulates metabolism through adipose-dependent and -independent mechanisms. *Cell Metab.* **25**, 935–944.e4 (2017).
 73. Scheele, C. & Wolfrum, C. Brown adipose crosstalk in tissue plasticity and human metabolism. *Endocr. Rev.* **41**, 53–65 (2020).
 74. Kahn, C. R., Wang, G. & Lee, K. Y. Altered adipose tissue and adipocyte function in the pathogenesis of metabolic syndrome. *J. Clin. Invest.* **129**, 3990–4000 (2019).
 75. Calles-Escandón, J. Insulin dissociates hepatic glucose cycling and glucagon-induced thermogenesis in man. *Metabolism* **43**, 1000–1005 (1994).
 76. Tan, T. M. et al. Coadministration of glucagon-like peptide-1 during glucagon infusion in humans results in increased energy expenditure and amelioration of hyperglycemia. *Diabetes* **62**, 1131–1138 (2013).
 77. Salem, V. et al. Glucagon increases energy expenditure independently of brown adipose tissue activation in humans. *Diabetes Obes. Metab.* **18**, 72–81 (2016).
 78. Whytock, K. L. et al. Prolonged glucagon infusion does not affect energy expenditure in individuals with overweight/obesity: a randomized trial. *Obesity* **29**, 1003–1013 (2021).
 79. Lee, W. H. et al. Hepatic insulin receptor: new views on the mechanisms of liver disease. *Metabolism* **145**, 155607 (2023).
 80. Loomba, R., Friedman, S. L. & Shulman, G. I. Mechanisms and disease consequences of nonalcoholic fatty liver disease. *Cell* **184**, 2537–2564 (2021).
 81. Bergman, R. N. et al. Hypothesis: role of reduced hepatic insulin clearance in the pathogenesis of type 2 diabetes. *Diabetes* **68**, 1709–1716 (2019).
 82. Castro, A. V. et al. Obesity, insulin resistance and comorbidities? Mechanisms of association. *Arq. Bras. Endocrinol. Metab.* **58**, 600–609 (2014).
 83. Boland, B. B. et al. Pancreatic β -cell rest replenishes insulin secretory capacity and attenuates diabetes in an extreme model of obese type 2 diabetes. *Diabetes* **68**, 131–140 (2019).
 84. Mauvais-Jarvis, F., Arnold, A. P. & Reue, K. A guide for the design of pre-clinical studies on sex differences in metabolism. *Cell Metab.* **25**, 1216–1230 (2017).
 85. Berglund, E. D. et al. Glucose metabolism in vivo in four commonly used inbred mouse strains. *Diabetes* **57**, 1790–1799 (2008).
 86. Ayala, J. E. et al. Considerations in the design of hyperinsulinemic-euglycemic clamps in the conscious mouse. *Diabetes* **55**, 390–397 (2006).
 87. Sawicki, K. T. et al. Hepatic tristetraproline promotes insulin resistance through RNA destabilization of FGF21. *JCI Insight* **3**, e95948 (2018).
 88. Finegood, D. T., Bergman, R. N. & Vranic, M. Estimation of endogenous glucose production during hyperinsulinemic-euglycemic glucose clamps. Comparison of unlabeled and labeled exogenous glucose infusates. *Diabetes* **36**, 914–924 (1987).
 89. Steele, R. et al. Measurement of size and turnover rate of body glucose pool by the isotope dilution method. *Am. J. Physiol.* **187**, 15–24 (1956).
 90. Kraegen, E. W. et al. Dose-response curves for in vivo insulin sensitivity in individual tissues in rats. *Am. J. Physiol.* **248**, E353–E362 (1985).
 91. Hasenour, C. M. et al. Mass spectrometry-based microassay of (2)H and (13)C plasma glucose labeling to quantify liver metabolic fluxes in vivo. *Am. J. Physiol. Endocrinol. Metab.* **309**, E191–E203 (2015).
 92. Young, J. D. INCA: a computational platform for isotopically non-stationary metabolic flux analysis. *Bioinformatics* **30**, 1333–1335 (2014).
 93. Hughey, C. C. et al. Loss of hepatic AMP-activated protein kinase impedes the rate of glycogenolysis but not gluconeogenic fluxes in exercising mice. *J. Biol. Chem.* **292**, 20125–20140 (2017).
 94. Chan, T. M. & Exton, J. H. A rapid method for the determination of glycogen content and radioactivity in small quantities of tissue or isolated hepatocytes. *Anal. Biochem.* **71**, 96–105 (1976).
 95. Yang, D. et al. Assay of low deuterium enrichment of water by isotopic exchange with [U-13C3]acetone and gas chromatography-mass spectrometry. *Anal. Biochem.* **258**, 315–321 (1998).
 96. Bederman, I. R. et al. Triglyceride synthesis in epididymal adipose tissue: contribution of glucose and non-glucose carbon sources. *J. Biol. Chem.* **284**, 6101–6108 (2009).
 97. Previs, S. F. et al. Using [(2)H]water to quantify the contribution of de novo palmitate synthesis in plasma: enabling back-to-back studies. *Am. J. Physiol. Endocrinol. Metab.* **315**, E63–e71 (2018).
 98. Burgess, S. C. et al. Impaired tricarboxylic acid cycle activity in mouse livers lacking cytosolic phosphoenolpyruvate carboxykinase. *J. Biol. Chem.* **279**, 48941–48949 (2004).
 99. Antoniewicz, M. R., Kelleher, J. K. & Stephanopoulos, G. Measuring deuterium enrichment of glucose hydrogen atoms by gas chromatography/mass spectrometry. *Anal. Chem.* **83**, 3211–3216 (2011).
 100. Boland, B. B. et al. Peptide-YY(3-36)/glucagon-like peptide-1 combination treatment of obese diabetic mice improves insulin sensitivity associated with recovered pancreatic β -cell function

- and synergistic activation of discrete hypothalamic and brainstem neuronal circuitries. *Mol. Metab.* **55**, 101392 (2022).
101. The, M. et al. Fast and accurate protein false discovery rates on large-scale proteomics data sets with percolator 3.0. *J. Am. Soc. Mass Spectrom.* **27**, 1719–1727 (2016).
 102. Käll, L. et al. Semi-supervised learning for peptide identification from shotgun proteomics datasets. *Nat. Methods* **4**, 923–925 (2007).
 103. Marx, H. et al. A large synthetic peptide and phosphopeptide reference library for mass spectrometry-based proteomics. *Nat. Biotechnol.* **31**, 557–564 (2013).
 104. Shackelford, C. et al. Qualitative and quantitative analysis of nonneoplastic lesions in toxicology studies. *Toxicol. Pathol.* **30**, 93–96 (2002).
 105. Alarcon, C. et al. Pancreatic β -cell adaptive plasticity in obesity increases insulin production but adversely affects secretory function. *Diabetes* **65**, 438–450 (2016).
 106. Bolger, A. M., Lohse, M. & Usadel, B. Trimmomatic: a flexible trimmer for Illumina sequence data. *Bioinformatics* **30**, 2114–2120 (2014).
 107. Dobin, A. et al. STAR: ultrafast universal RNA-seq aligner. *Bioinformatics* **29**, 15–21 (2013).
 108. Liao, Y., Smyth, G. K. & Shi, W. featureCounts: an efficient general purpose program for assigning sequence reads to genomic features. *Bioinformatics* **30**, 923–930 (2014).
 109. Love, M. I., Huber, W. & Anders, S. Moderated estimation of fold change and dispersion for RNA-seq data with DESeq2. *Genome Biol.* **15**, 550 (2014).
 110. The Gene Ontology resource: enriching a GOld mine. *Nucleic Acids Res.* **49**, D325–D334 (2021).
 111. Ashburner, M. et al. Gene ontology: tool for the unification of biology. *Nat. Genet.* **25**, 25–29 (2000).
 112. Carbon, S. et al. AmiGO: online access to ontology and annotation data. *Bioinformatics* **25**, 288–289 (2009).

Acknowledgements

The authors wish to thank the Animal Sciences and Technologies staff at AstraZeneca for their assistance with animal husbandry and care, Maria Ryaboshapkina for supporting RNA-seq data upload to GEO, and the University of Chicago Advanced Electron Microscopy Core Facility (RRID:SCR_019198). The authors thank Vanderbilt MMPC and Vanderbilt Analytical Assay Core and their NIH funding, DK135073 and DK020593, respectively, as well as S10OD025199 for stable isotope and metabolic flux analysis. The Villum Center for Bioanalytical Sciences at the University of Southern Denmark is acknowledged for access to high-end MS instruments.

Author contributions

R.C.L., S.E., S.W., L.L., O.P.M., and C.J.R. designed experiments; R.C.L., S.E., S.W., K.K., L.L., O.P.M., C.B., N.B., S.O., A.A., X.L., T.K., S.K., S.S., and

M.R.L. collected and/or analysed and interpreted experimental data; G.P. and A.-C.A. provided pathology analysis of mouse studies; R.C.L., S.E., and C.J.R. wrote the paper; S.W., S.K., O.P.M., and M.R.L. reviewed and edited the manuscript.

Competing interests

R.C.L., C.J.R., S.W., S.O., A.C.-A., S.K., S.E., N.B., and A.A. are current employees of AstraZeneca and may own stock in AstraZeneca. K.K., S.S., X.L., C.B., and G.P. are former employees and may also own stock in AstraZeneca. T.K. and M.R.L. have received research support from AstraZeneca. The remaining authors declare no competing interests.

Additional information

Supplementary information The online version contains supplementary material available at <https://doi.org/10.1038/s41467-025-59773-4>.

Correspondence and requests for materials should be addressed to Rhianna C. Laker or Christopher J. Rhodes.

Peer review information *Nature Communications* thanks Jonathan Campbell, Gianluca Iacobellis and the other, anonymous, reviewer(s) for their contribution to the peer review of this work. A peer review file is available.

Reprints and permissions information is available at <http://www.nature.com/reprints>

Publisher's note Springer Nature remains neutral with regard to jurisdictional claims in published maps and institutional affiliations.

Open Access This article is licensed under a Creative Commons Attribution-NonCommercial-NoDerivatives 4.0 International License, which permits any non-commercial use, sharing, distribution and reproduction in any medium or format, as long as you give appropriate credit to the original author(s) and the source, provide a link to the Creative Commons licence, and indicate if you modified the licensed material. You do not have permission under this licence to share adapted material derived from this article or parts of it. The images or other third party material in this article are included in the article's Creative Commons licence, unless indicated otherwise in a credit line to the material. If material is not included in the article's Creative Commons licence and your intended use is not permitted by statutory regulation or exceeds the permitted use, you will need to obtain permission directly from the copyright holder. To view a copy of this licence, visit <http://creativecommons.org/licenses/by-nc-nd/4.0/>.

© The Author(s) 2025

Rhianna C. Laker^{1,6}✉, **Shaun Egolf**^{1,6}, **Sarah Will**¹, **Louise Lantier**², **Owen P. McGuinness**², **Charles Brown**³, **Nicholas Bhagroo**¹, **Stephanie Oldham**¹, **Kyle Kuszpit**³, **Alex Alfaro**³, **Xidan Li**⁴, **Taewook Kang**⁵, **Giovanni Pellegrini**⁴, **Anne-Christine Andréasson**⁴, **Sarina Kajani**¹, **Sadichha Sitaula**¹, **Martin R. Larsen**⁵ & **Christopher J. Rhodes**¹✉

¹Research and Early Development, Cardiovascular, Renal and Metabolism, BioPharmaceuticals R&D, AstraZeneca, Gaithersburg, MD, USA. ²Vanderbilt University Mouse Metabolic Phenotyping Center, Nashville, TN, USA. ³Imaging and Data Analytics, Clinical Pharmacology and Safety Sciences, AstraZeneca, Gaithersburg, MD, USA. ⁴Research and Early Development, Cardiovascular, Renal and Metabolism, BioPharmaceuticals R&D, AstraZeneca, Gothenburg, Sweden. ⁵Department of Biochemistry and Molecular Biology, PR group, University of Southern Denmark, Odense, Denmark. ⁶These authors contributed equally: Rhianna C. Laker, Shaun Egolf. ✉e-mail: rhianna.laker@astrazeneca.com; christopher.rhodes@astrazeneca.com